Design and Manufacturing of All-dielectric Optical Metamaterial with Gradient Index of Refraction

by

Chih-Hung Hsieh

B.S., Power Mechanical Engineering,
National Tsing Hua University, Taiwan (2005)

S.M., Electronics Engineering
National Tsing Hua University, Taiwan (2007)

Submitted to the Department of Mechanical Engineering
in partial fulfillment of the requirements for the degree of

Doctor of Philosophy

at the

MASSACHUSETTS INSTITUTE OF TECHNOLOGY

June 2015

Signature redacted

Author .....
Department of Mechanical Engineering
March 6, 2015

Signature redacted

Certified by .....
George Barbastathis
Professor of Mechanical Engineering
Thesis Supervisor

Signature redacted

Accepted by .....
David E. Hardt
Chairman, Department Committee on Graduate Theses

Design and Manufacturing of All-dielectric Optical Metamaterial with Gradient Index of Refraction

by

Chih-Hung Hsieh

Submitted to the Department of Mechanical Engineering
on March 6, 2015, in partial fulfillment of the
requirements for the degree of
Doctor of Philosophy

Abstract

Gradient index (GRIN) materials offer the most general manipulation over wave fields of light compared to conventional refractive optics, where the light is deflected by the curved surface. The creative way to implementing GRIN optics is to construct a subwavelength structure with the electromagnetic characteristics that are unavailable via the natural material. This artificial GRIN structure also known as "metamaterial" can be classified into two general categories: film and slab GRIN optics, depending on the propagation direction of light penetrating through or propagating along the metamaterial.

In this dissertation, two different purposes of all-dielectric GRIN optics on (1) film: light extraction enhancement of the scintillator; (2) slab: aberration-free focusing using Lüneburg lens, are both investigated. The scintillator made by ceramics like Lutetium Yttrium Orthosilicate (LYSO) possesses higher index of refraction at 1.82 than the surrounding environment, which causes extraction loss due to index mismatching and total internal reflection (TIR) from scintillator to photodetector. A hybrid structure including two-dimensional photonic slab covered by the nanocone structure on the top was devised to recycle the energy loss from TIR and to create an index-matching layer in between. Design parameters of the hybrid structure were optimized by the simulation based on rigorous coupled-wave analysis, and the fabrication of hybrid structure was patterned by nanospheres (for nanocone structure) and laser interference (for photonic slab) lithography, respectively. Reactive ion etching (RIE) facilitated pattern transfer after two separate lithography processes. Finally, the characterization of nanostructured scintillator was performed with the ionizing source.

The rest of this research focuses on the implementation of the slab GRIN optics: Nanostructured Lüneburg lens. The Lüneburg lens is an aberration-free lens that can perfectly focus light on the opposite edge of the lens area, and such property can be used for light coupling from fiber to waveguide in the Silicon photonics. We designed the nanostructured Lüneburg lens on the silicon-on-insulator substrate using effective index of refraction computed by photonic band theory, and the fabrication was

carried out by the e-beam lithography and RIE process. The device characterized by near-field scanning optical microscopy exhibited the single focusing behavior under fundamental mode illumination via the intensity map over the lens region. In addition, the bi-foci phenomenon under higher order mode illumination was also revealed in the finite difference time domain simulation, and the ray picture for explaining the bi-foci was also included using Wigner distribution function and Hamiltonian ray-tracings.

Thesis Supervisor: George Barbastathis Signature redacted
Title: Professor of Mechanical Engineering

Acknowledgments

My favorite quote from Mahatma Ghandhi "First they ignore you, then they laugh at you, then they fight with you, then you win" – is the best portrait of my entire graduate life since I was still a research rookie in National Tsing Hua University. It is a struggling period during the exploration of any research, and I could not have done this great accomplishment without the assistance from people working along with me.

I would like to thank Prof. George Barbastathis for initializing my research life at MIT. George offered me the opportunity to learn from his academic insight, and guided me through to break the ground I have not exposed to. He behaved as a strict teacher to insufficient aspects in my research, but always played as an attentive mentor for our need while pursuing the scientific truth. Working with George opens up my vision of life.

I also thank Prof. Nicholas Xuanlai Fang and Karl Berggren for serving on my committee. Nick always pulls me out by invaluable experience and suggestion when I feel like sinking into the vortex of research puzzles. The discussion with Nick enriches details of this thesis. Karl came to me for showing his abundant experience on fabrication work, especially in demonstrating each process with a sound physical ground instead of the black magic.

I would like to thank my lab mates in 3D optical system group. Dr. Lei Tian is my best mentor in peers. Thoughts and reminders from him walk me through the challenge in my graduate life. Dr. Hanhong Gao sets a solid foundation for this work with his brilliant work and help. Yi Liu accompanies with me for the tough time during research with her happy smile forever. Jeong-gil Kim is the best buddy in preparing quals and defense. His discussion advances part of this work forward. Justin Lee shares his MIT tips all the time. I would never forget the Thanksgiving time we spent together. Dr. Hyungryul Choi and Dr. Se-Young Yang kindly showed me the basic skills and fruitful tricks to conduct a successful process in the fab. They instruct me the fabrication 101 in NSL. Dr. Nader Shaar gave me useful conversations

when I was lost halfway to my degree. I deeply appreciate his encouragement. Dr. Anthony Nichol surprised me by his entrepreneurship and his "great idea" on my first group presentation.

Strengths from the Taiwanese community held me up. Chia-Hsin Chen feeds me food and coffee to extend my energy on doing endless research load. We also definitely were the best partner in the basketball game. Jiun-Yih Kuan, Wei-Chun Hsu, and Miss Pan Pan and I not only gather for nice food and happy hour, but also engrave the unforgettable memory in our life. Yi-Heng Sen is the best consulting man when pursuing my future career. He taught me the secret in applying a job.

Special thanks to Dr. Yen-Sheng Lu and Dr. Chia-Ming Chang. Yen-Sheng played the role as my comrade-in-arms in NTHU and MIT. We've been collaborating over years, and continue our intersection in both future career. Chia-Ming was the man inspiring me for study abroad, and he is also the mentor who pass the ball to me for the buzzer-beat of my thesis.

Last, my sincere appreciation to my parents and my fiancee, Yunchia Liang. My parents, Huan-Hsu Hsieh and Chun-Mei Hsu raised me up in an austere and ordinary way but with their simple and correct philosophy. That's why I never deviate from the integrity. Yunchia came to me as an angel since I was 16 year-old. She stood with me through the challenges in my life. She never left from me whenever I need her. She's the one and the only one in my life.

Contents

THIS PAGE INTENTIONALLY LEFT BLANK

List of Figures

List of Tables

THIS PAGE INTENTIONALLY LEFT BLANK

Chapter 1

Introduction

Contents

Gradient Index (GRIN) materials offer the most general possibilities for the manipulation of light. Applications of GRIN materials include focusing in imaging systems, guiding in optical fibers, light trapping structures for solar cells, light extraction from light emitting devices (LED), etc. Generally, these applications can be classified as two categories: film and slab GRIN optics, depending on the light that penetrates through or propagates along the GRIN medium.

In this dissertation, two devices from both categories were studied: (1) Surface engineering of the scintillator for light extraction enhancement (2) Nanostructured Lüneburg lens implementation. In this chapter, a brief introduction to film and slab GRIN materials will be shown in the beginning followed by their problem definition in the ongoing sections. Last, the architecture of this dissertation will be discussed in the final section.

1.1 Gradient-index Metamaterials

The interaction between the light and medium strongly depends on the propagation direction of light as shown in Fig. 1-1, which will decide the way how to engineering the material for GRIN purpose. Many GRIN applications require large variation of refractive index, so fabricating the structure around the scale of desirable wavelength would yield wider implementation margin than using traditional ion exchange or stuffing method in the fiber manufacturing. The novel device made by structuring natural materials to create the artificial electromagnetic characteristic is entitled with a name of "metamaterial" now because it hardly could be replaced with any other materials in nature. Benefits of GRIN metamaterials include better light retention due to all-dielectric implementation and compatibility with Si photonics system for coupling and processing of light. In general, the procedure of creating the GRIN metamaterial consists of (1) Analyze the index of refraction in the ambience around the device (2) Choose materials with proper index of refraction fit to the design requirement and fabrication process (3) Simulate and verify the performance of the GRIN metamaterial (4) Perform the fabrication (5) Characterize the GRIN metamaterial. Because of the difference between applications, the flow could be modified to

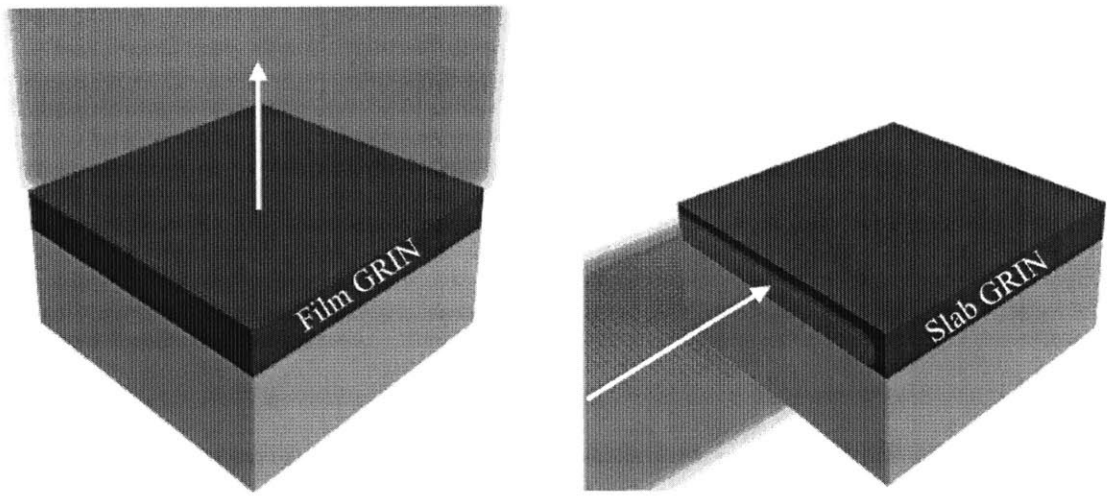

(a) (b)

Figure 1-1: Two different categories of GRIN metamaterials (a) Slab GRIN (b) Film GRIN. The white arrows indicates the propagation direction of light.

meet the implementation.

1.2 Film gradient-index optics

The film GRIN optics in this dissertation mainly represents applications for antireflection and light extraction enhancement. They both penetrate the film through for the purpose of light collection but with opposite propagation direction. An optimum design can not be used reversibly in this case due to index of refraction at emission point of light. When the light is going from low-index ambience to high-index substrate, the problem normally tackles the impedance matching only. However, if the condition is reversed, *i.e.* the light is going from high-index substrate to low-index ambience, the total internal reflection (TIR) should be considered together with impedance matching for the light beyond the critical angle. One of antireflective applications is the light trapping structure for enhancing solar cell efficiency as shown in Fig. 1-2 [5, 6]. After nano-texturing the surface of the silicon substrate, the reflectivity can decrease down to 0.52% compared to the 25% of that results from traditional micro-texture. In addition, the nanocone structure also shows the same antireflection ability for large-angle incidence of light. However, the nanocone structure will not work out on the light extraction application due to TIR, so a different structure like diffractive grating

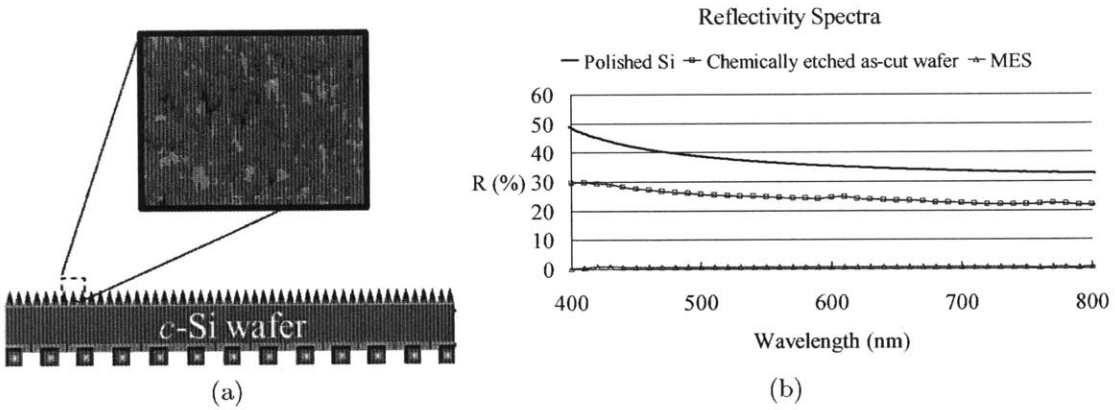

(a) (b)

Figure 1-2: Moth-eye structure (a) Application on an ultrathin monocrystal Si solar cell (b) Reflectivity over visible band between 400-800 nm.

is needed to break the TIR restriction. Take the case of light extraction from LED for instance. The light emitting layer is normally grown on the sapphire substrate with index of refraction around 1.8, which results in a critical angle of 34°. The light with incident angle beyond 34° will not be transmitted out from the sapphire, and is trapped to reflect back and forth within the substrate until energy dissipated. A photonic crystal as a two dimensional (2D) grating that is shown in Fig. 1-3 helps the extraction of light beyond critical angle [7, 8], but the trade-off is the less transmission for incident angle smaller than critical angle. Thus, a hybrid structure combining the antireflection for the light below critical angle and diffraction to break the TIR will be demonstrated in the chapter 2 of this dissertation.

1.3 Slab gradient-index optics

In slab GRIN optics, the light satisfying the guiding condition propagates along the waveguide for silicon photonics applications such as coupling and focusing. There are three famous and interesting examples of GRIN lens that have been studied well: Maxwell-fish eye, Lüneburg, and Eaton lens as shown in Fig. 1-4. Here are their description of functionality: (1) Maxwell's fish-eye lens: If a point source is at the edge of the lens, those rays with direction pointing toward the lens region will focus right at the opposite edge again (2) Lüneburg lens can perfectly focus the incoming

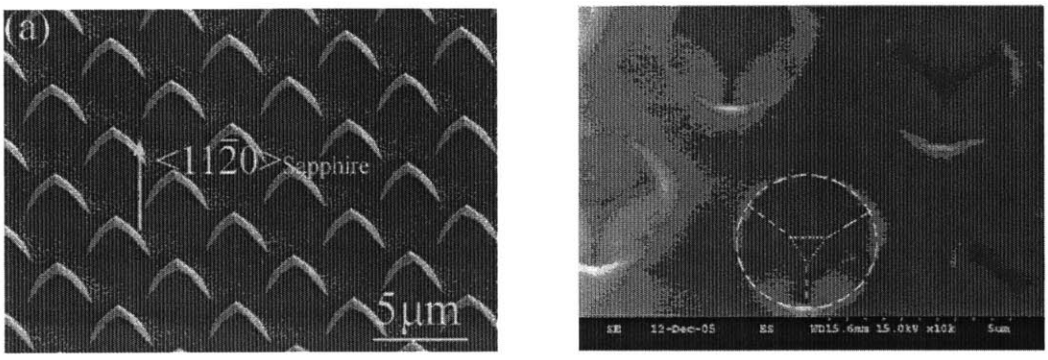

(a) (b)

Figure 1-3: Patterned sapphire structure for light extraction enhancement (a) Pyramid [7] (b) Inverted pyramid [8].

plan wave from any direction to the opposite edge of the lens region (3) Eaton lens: the retro-reflector for bending the light with desirable degrees. The refractive index distribution of these GRIN lens follows:

$$\text{Maxwell's fish-eye}: \qquad n(r) = \frac{n_o}{1+\left(\frac{r}{R}\right)^2} \tag{1.1}$$

$$\text{Lüneburg}: \qquad n(r) = n_o\sqrt{2-\left(\frac{r}{R}\right)^2} \tag{1.2}$$

$$180^\circ \text{ Eaton}: \qquad n(r) = n_o\sqrt{\frac{2R}{r}-1} \tag{1.3}$$

where n_o is ambient index of refraction outside the lens region, R is the radius of the lens region, and r is the radial polar coordinate with the lens center as origin. The Lüneburg lens is the most applicable components in three of them because it has reasonable index variation in terms of fabrication and practical functionality. The benefit of Lüneburg lens is omnidirectional focusing; however, exact implementation of this GRIN profile had, until recently, been available in microwave frequencies only for applications such as focusing into high-gain antennas [10, 9, 11]. People con-

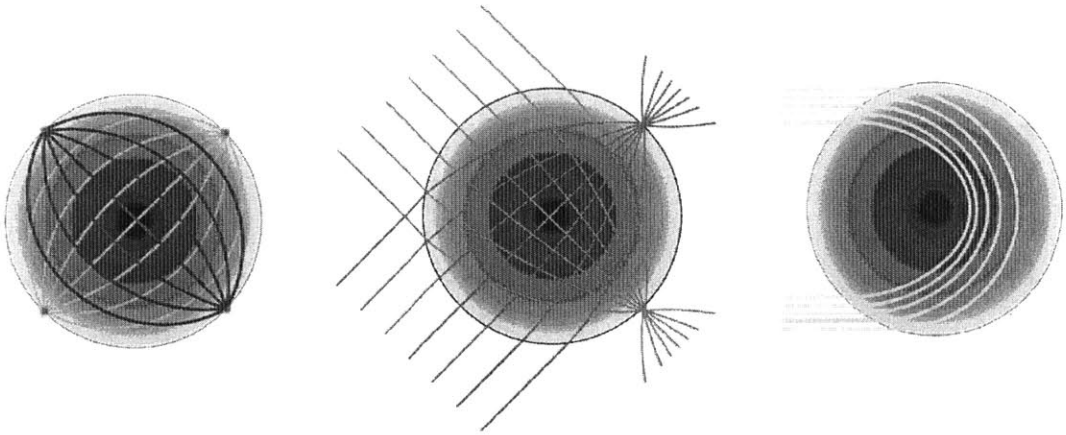

(a) (b) (c)

Figure 1-4: Examples of GRIN lens (a) Maxwell's fish-eye lens (b) Lüneburg lens (c) 180° Eaton lens. Color lines denotes the ray path through the lens region.

trolled the index of refraction using layered material to build up the Lüneburg lens in macro-scale. By exploiting nanolithography and fundamental understanding of refractive index manipulation through dispersion, infrared Lüneburg lenses have also been successfully demonstrated. For example, Yao *et al* varied the thickness of the thin film to control the effective index of refraction (EIR) of the Lüneburg lens, but the mode of the device becomes ill confined within the device layer due to relatively small thickness [12]. A recent example of gradient-thickness dielectric Lneburg lens using gray scale lithography by focus ion beam is shown in Figure 1-6 [13]. The same concept of using gradient-thickness dielectrics can be also applied to plasmonic Lüneburg lens to create desirable mode index, but the intrinsic propagation loss from the metal surface is still incompatible with that in silicon photonics even using optically pumped gain medium [14, 15]. The Lüneburg lens is a great interface to mitigate the misalignment while coupling the light from a fiber to silicon photonics, but a design that is compatible with current manufacturing of the silicon photonic system has not been fulfilled. Chapter 3 in this dissertation will demonstrate the process of implementing an Lüneburg lens using the nanostructured film that is compatible to the current manufacturing of silicon photonics.

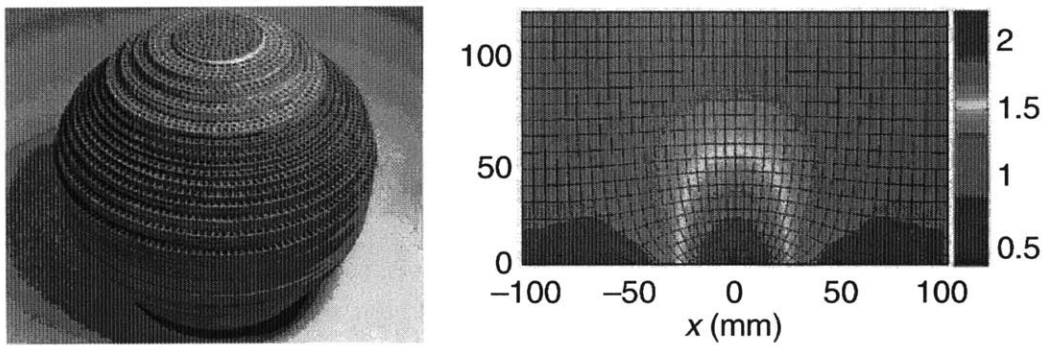

(a) (b)

Figure 1-5: Flattened Lüneburg lens for microwave frequencies (a) Fabricated 3D lens (b) Index distribution along one vertical slice [9].

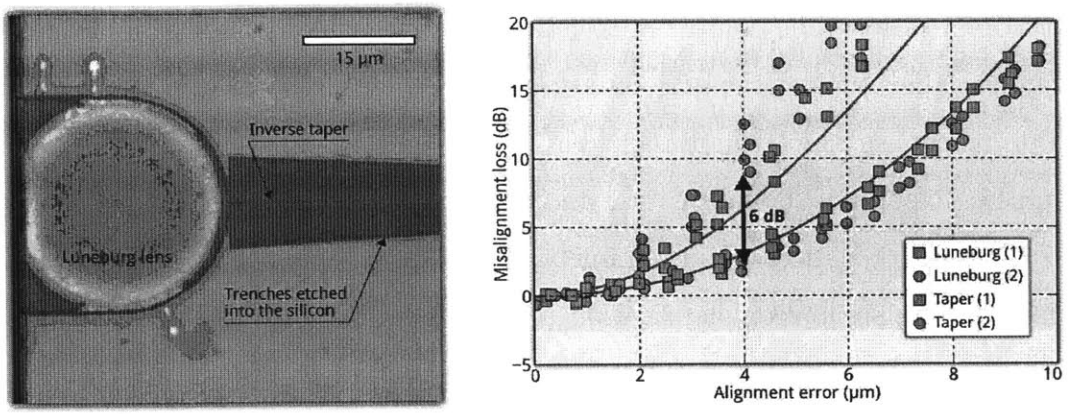

(a) (b)

Figure 1-6: Gradient-thickness Lüneburg lens (a) Optical image of the fabricated sample (b) Alignment results of light coupling from optical fiber to single-mode waveguide: with and without Lüneburg lens [13].

1.4 Thesis Architecture

Chapter 2 studies the hybrid structure for light extraction enhancement of the X-ray scintillator. This hybrid structure consist of a 2D photonic grating covered by nanocones. The optimization process utilizes rigorous coupled wave analysis for different models at the design level because of the good approximation and relatively

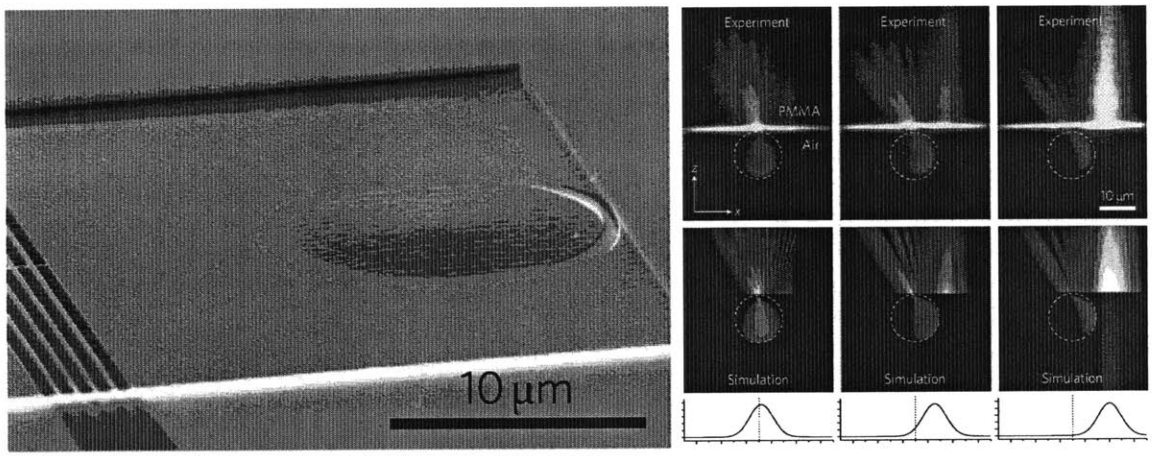

(a) (b)

Figure 1-7: Plasmonic Lüneburg lens (a) Device SEM. The PMMA layer with gradient-thickness patterned by grey-scale e-beam lithography was deposited on top of the gold layer (b) Experiment and simulation with different excitation conditions [14].

shorter computation time compared to finite difference time domain simulation. By sweeping variables such as the periodicity and duty cycle of photonic gratings and the height of nanocones, the optimum for light extraction from different ambience can be determined. Results of the fabrication and characterization will also be summarized.

An all-dielectric nanostructured Lüneburg lens has not been presented completely including design, simulation, fabrication and characterization until the accomplishment in this work. Chapter 3 will introduce the work of nanostructured Lüneburg lens carried out by other researchers previously from our group, and show the entire flow of implementation. Two design based on an array of nano rods and holes will be covered, and challenges resulting from the fabrication of the rod-slab case is also included. In addition, the near-field observation of nanostructured Lüneburg lens is shown for the first time, and the analysis of the measured image using finite difference time domain and Hamiltonian ray-tracing simulation are performed to explain characterization results.

Finally, a concluding remark and future work will be summarized in chapter 4.

Chapter 2

Light Efficiency Enhancement of the Scintillator

Contents

2.1 Intorduction

2.1.1 Scintillation absorption and process

The ionizing radiation carries energy that can ionize the material including subatomic particles, ion, or atoms moving at relativistic speeds, and electromagnetic waves on the high energy end of the electromagnetic spectrum [16]. From the high energy physics, X-ray security, to positron emission tomography, plenty of applications rely on the scintillator to convert the ionizing radiation to non-ionizing radiation that is the feed for commercially available detector such as PhotoMultiplier Tube (PMT)

or Avalanche PhotoDetector (APD). The scintillator is a material that can emit the light by ionizing event happened inside the material after receiving ionizing radiation illumination. Mechanisms of the scintillation absorption consist of [1]:

- **Heavy charged particles**: the inelastic collision between impinging particles at relativistic speed and the electrons of scintillator crystals can deposit the partial energy from the energetic particle to the local medium, which can be described by Bethe formula as [17]

$$-\frac{dE}{dx} = \frac{4\pi e^4 z^2}{m_e c^2 \beta^2}\left[\ln\left(\frac{2m_e c^2\beta^2}{I(1-\beta^2)}\right) - \beta^2\right], \tag{2.1}$$

  where the loss of total energy E along the penetration direction x within a homogeneous medium with a density of N atoms/cm^3 and each atom of the atomic number Z is assumed here. I is an empirical constant and corresponds to the mean excitation and ionization potential of the scintillator. M is the rest mass of the particle, z is the particle charge, β is velocity ($V = \beta c$) and m_e and e are the rest mass of an electron and the electronic charge, respectively. For the non-relativistic case($\beta \ll 1$) the last two terms in the bracket can be neglected.

- **Electrons**: Impinging electrons with high energy ($> MeV$) deposit their energy also in radiative form while they are deviated or deflected by the nuclei.

- **Electronmagnetic radiation**

  1. **Compton effect**: an elastic collision between photon and a nearly free electron inside the scintillator. The electron acquired the kinetic energy from recoil force or the impinging particle or high energy radiation.
  2. **Photoelectric effect**: the photon was absorbed by a bound electron in the inner shell of atom.

- **Neutron**: acquiring the energy from recoil force by the similar process with Compton effect.

Moreover, the scintillation process will involve aforementioned absorption resulting in re-emission at the visible band. When the impinging energy of particles or rays is larger than 100 keV, absorption happens in the inner shell (K or L shell) to generate the hole-electron pairs. The relaxation process of holes and electrons differs. The deep hole can be filled up by another electron in the atom to emit the light with a shallow hole generation, and the energetic electron within crystal, that is Auger electron, could also be generated during the relaxation. Both the radiative photon and Auger electron can generate the new hole-electron pairs until the energy of new electrons smaller than the ionization energy. Each relaxation of the electron-hole pair radiates a photon out, which provides the necessary conversion from ionizing to non-ionizing radiation.

2.1.2 Light yield

The conversion efficiency of the scintillation can be simply described as:

$$\eta = \frac{N_{\text{ph}}}{N_{\text{eh,max}}} = \frac{N_{\text{eh}}}{N_{\text{eh,max}}} \times \frac{N_{\text{ph}}}{N_{\text{eh}}} = \beta SQ \tag{2.2}$$

where the η represents the conversion efficiency of the scintillator. N_{ph} and $N_{\text{eh,max}}$ are the number of extracted photons, available e-h pair for conversion, maximum electron-hole pairs generated within the scintillator, respectively. β is e-h the conversion efficiency function of materials, namely $N_{\text{eh}}/N_{\text{eh,max}}$. S and Q indicate the energy transfer of e-h pairs and quantum efficiency of the luminescence center, respectively. The product of SQ is equal to $N_{\text{ph}}/N_{\text{eh}}$. In fact, a more powerful index for evaluating conversion efficiency is the light yield (LY), which is the total photon number generated per unit illumination energy. Using a series of simplification by substituting other parameters, the absolute LY is expressed as [1]:

$$LY_{abs} = \beta \frac{SQ}{E_g} \tag{2.3}$$

Therefore, the LY is proportional to the total extracted photon number as well as the channel number of the multichannel analyzer, so it could be simply expressed by the peak variation of the channel number. More details about characterization and post-analysis will be discussed later.

2.1.3 Problem Definition

Light extraction from scintillators is one of the challenges in scintillator applications due to the relatively high refractive index of scintillators compared to the output environment. Total Internal Reflection (TIR) restricts the emitted light from scintillator that can couple out to the detector end. The same problem also happens in light extraction from light emitting device (LED) due to high index of refraction of the substrate. The solution to breaking the TIR usually utilizes a diffractive grating, sometimes referred to as "photonic crystal", to diffract out the light beyond the critical angle. A. Knapitsch *et al* have facilitated the extraction efficiency by a 2D photonic crystal fabricated on lutetium oxyorthosilicate (LSO) crystal as shown in Figure 2-1(a) [18]. They patterned the Si_3N_4 deposited on top of the LSO substrate

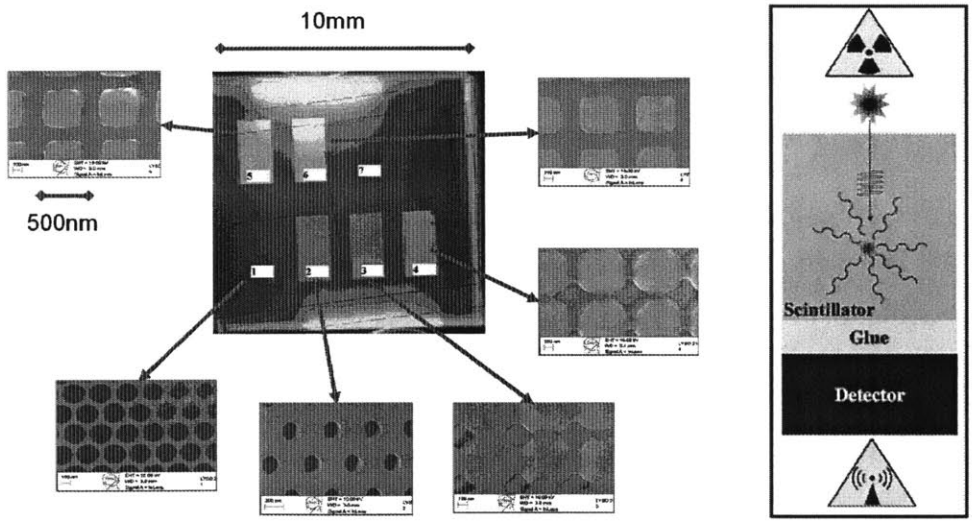

(a) (b)

Figure 2-1: Light extraction from Scintillator (a) Fabrication results from [1]. [Note: RI denotes Refractive Index.] (b) The general usage of scintillator coupled with the PMT using the optical glue.

using e-beam lithography and reactive ion etching (RIE) because of the difficulty of directly plasma etching on scintillators and the refractive index of Si_3N_4 nearly matching that of the scintillator. Results with optimized structure stack showed 56% gain of photon extraction while coupling the light from LSO to air. However, the scintillator is usually coupled with the PMT window using optical glue whose index is the same as the PMT window as shown in Fig. 2-1(b). The design for coupling light to air is not practical in applications.

Herein, the design of the structure should consider the refractive index at extraction plane as that in PMT window instead of air coupling. Moreover, a similar crystal compared to LSO, Cerium-doped Lutetium Yttrium Orthosilicate (LYSO:Ce), was used in this work as the substrate because of several advantages such as non-hygroscopic, high light output and density, quick decay time, and excellent energy resolution. Consequently, the hybrid structure combining the diffractive and antireflective characteristics will be presented from design, optimization, fabrication and characterization based on LYSO crystals in the following sections.

2.2 Structure design and optimization

2.2.1 Hybrid Structure

The main idea of the hybrid structure is going to combine the benefit from antireflective nanocones and diffractive photonic crystals. However, the two goals conflict in the sense that the first function (reducing Fresnel reflection) requires a subwavelength pitch, whereas the second function (diffracting light that would otherwise be TIRed) requires a diffractive structure with period bigger than wavelength. Fortunately, if the period is near the wavelength, a mix of both effects can be observed [19, 20, 21], and we can hope to balance them effectively to maximize light extraction. Because both benefits are not a pure addition in the optical performance, the design of experiment is adopted for evaluating the best performance. Basically, the hybrid structure uses a photonic crystal as the backbone with cover of nanocones array. Three dif-

ferent hybrid structures were depicted in Figure 2-2: cone-cover, cone-topping, and cone-valley. Physically, the photonic crystal backbone will keep the diffractive characteristic to break the TIR, and nanocones could be the index-matching layer between photonic crystal and environment. In order to save computation time, the parameter optimization is carried out by a free simulation software: Stanford Stratified Structure Solver (S4) [22]. S4 is a frequency domain code to solve the linear Maxwells equations in layered periodic structures. Internally, it uses Rigorous Coupled Wave Analysis (RCWA; also called the Fourier Modal Method) and the S-matrix algorithm. S4 can compute the reflectivity, transmissivity, and diffraction efficiency in each order using transfer matrix method after layering the desirable design.

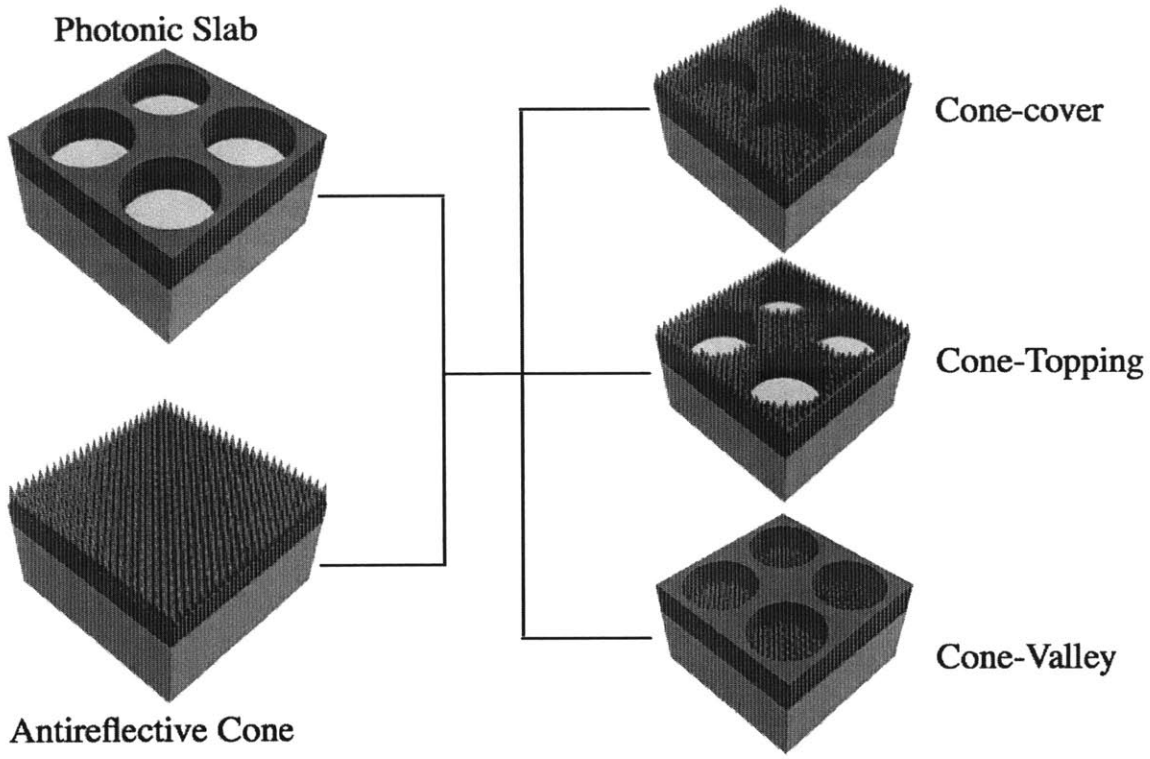

Figure 2-2: Three different hybrid structures sharing the photonic crystal as the backbone with the coverage of antireflective nanocones: Cone-cover, Cone-Topping, and Cone-Valley.

2.2.2 Parameter optimization

Before running the optimization, we need to consider the entire process from light emission to the extraction at exit plane. The light normally can be regarded as isotropic emission from the luminescence center if the scintillator is a homogeneous material. After emission, the light can bounce back and forth inside the scintillator if the incident angle is less than the critical angle. Hence, the probability of impinging photons on the extraction plane depends on the surrounding medium of the scintillator. Take the configuration of Fig.2-1(b) for example. The LYSO scintillator with refractive index of 1.82 is coupled to an optical glue with index of 1.41. One can simulate the angle distribution of impinging photons using freewares such as Geant4 and SLitrani based on the Monte Carlo method [23, 24]. Results as shown in Fig. 2-3 indicate only 28.9% of photons can be extracted directly or indirectly from the extraction plane [18]. The rest of emission photons are leaked out to the air or dissipated due to trapping inside the scintillator by TIR. In order to recycle the photons impinging to other facets, a diffusive teflon wrapping or coating is usually used for surrounding medium to reflect most of the emission light from the side back to the scintillator, whereas keeping the extraction plane clean for a good coupling.

The number of impinging photons for Air/LYSO interface as shown in the Fig. 2-4 was simulated by our collaborators in CERN (European Organization for Nuclear

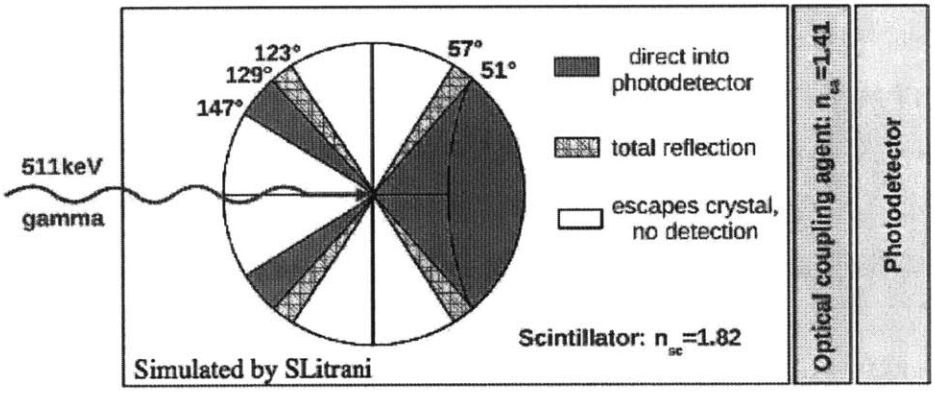

Figure 2-3: Angular distribution of emission photon inside the scintillator. Without any reflective wrapping, the photons escaping the scintillator from other facet of the crystal to the air causes the loss (white portion). In addition, part of the photon will be trapped until dissipation due to TIR (gray portion) [18].

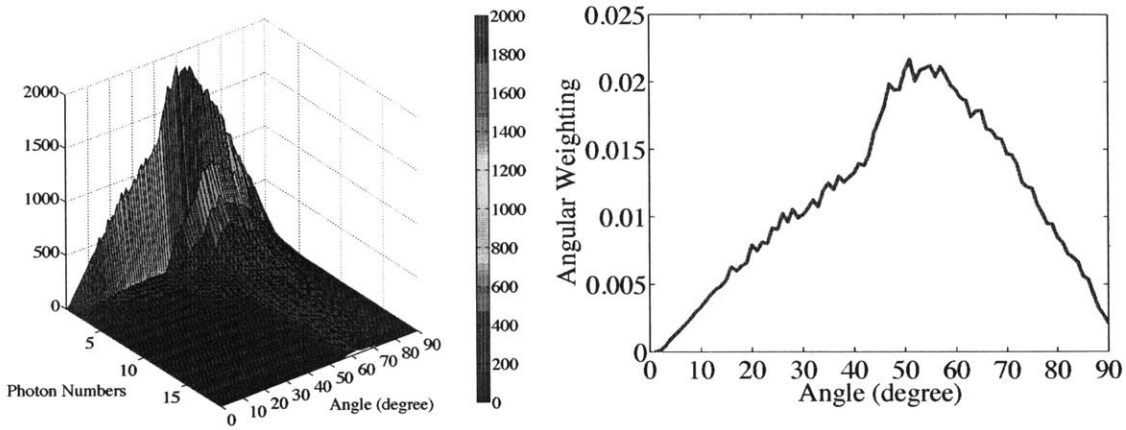

(a) (b)

Figure 2-4: Number of the impinging photons simulated using Monte-Carlo method by SLitrani for LYSO cylinder wrapping with teflon tape (a) Impinging counts is function of the angle and recursion (b) Angular weighting function by summing up the data for each angle and normalized to the total count of the photons.

Research) using SLitrani for LYSO cylinder wrapping with teflon tape. In the simulation, 100,000 photons were randomly generated within the LYSO substrate at the beginning of the simulation, and SLitrani counted the number of photons hitting the extraction plane recursively until they were extracted or extinct. Obviously, most of the photons hit the extraction plane at the incident angle around 55° while using teflon wrapping. Evaluting the number of photon extraction along with on the distribution of impinging photons makes more sense to final results, but it has difficulty to integrate the SLitrani and S4 together for simulation in reality. Nontheless, the distribution of impinging photons still can be used for optimization if two assumptions are made:

Table 2.1: Parameters for optimization.

Constants			
Si_3N_4 Index	2.06	LYSO Index	1.82
Parameters			
Photonic crystal		Nanocones	
Period	100–3000 nm	Period	100 nm
Duty Cycle	0–90%	Thickness	50–350 nm
Thickness	150–750 nm		

- The angular distribution of the impinging photons from the photonic crystal when coming back to the interface will have the same form as well as that in the grease (no structure) case. In fact, similar angular distribution of impinging photons for different medium at extraction plane remains in air and grease coupling as long as the teflon wrapping condition holds.

- The fraction of recuperated photons at each reflection on the extraction plane follows the similar pattern as well as that in the grease (no structure) case (81.6%, 82.7%, 83.4%...). This argument is also sound because it was observed that the angular distribution of the impinging photon strongly depends on the wrapping material instead of the medium surrounding the extraction plane.

In order to average out the variation between recurrences, the angular distribution of impinging photons could be summed up and normalized to get an angular weighting function, which is used with transmission data to compute efficiency maxima during the optimization.

Parameters affect the performance of the entire device were summarized in Table 2.1. The period of the nanocone was chosen as 100 nm that is fixed by the diameter of nanospheres in the fabrication. In addition, the definition of duty cycle remained the same as that in 1D case because it is more convenient to sweep the diameter instead of area linearly in the code. The other parameters were swept accordingly in the RCWA simulation to find the maximum of transmissivity. In S4 software, it is more effective to vary one periodicity per simulation, so the periodic nanocones will be accordingly replaced with an effective medium.

Thus, we need to verify this approximation before running through the whole optimization. The transmissivity of both cone and effective medium on top of a photonic crystal have been simulated as shown in Figure 2-5(a). The result for cone case is consistent with that for effective medium except little underestimation while the incident angle is less than 15°, but this variation could be neglected after considering the angular weighting of impinging photons as shown in Figure 2-5(b) due to low probability at around normal incidence. Herein, the entire process of optimization

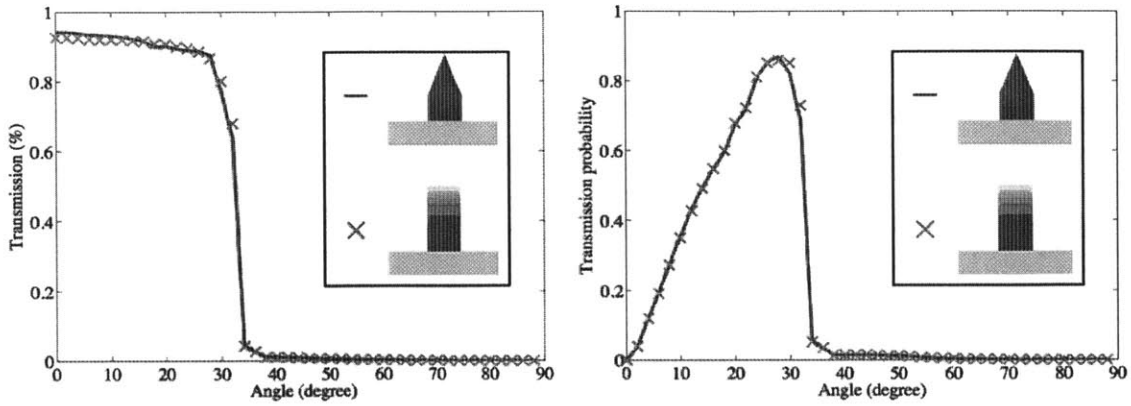

(a) (b)

Figure 2-5: Verification of the approximation between cone and effective medium on top of the photonic crystal using S4 simulation (a) Transmissivity (b) Transmission probability. The simulation parameters: 500 nm in pitch with 20% duty cycle. Thickness of the photonic crystal and cone are 500 and 350 nm, respectively. All schematics no to scale.

is to compute the efficiency gain compared to the bare Grease/LYSO interface and LYSO with photonic crystal. The duty cycle and pitch were swept for the specific thickness of photonic crystal and nanocone, respectively. An example of the result as shown in Figure 2-6 consists of the thickness of 150 and 350 nm for nanocone and

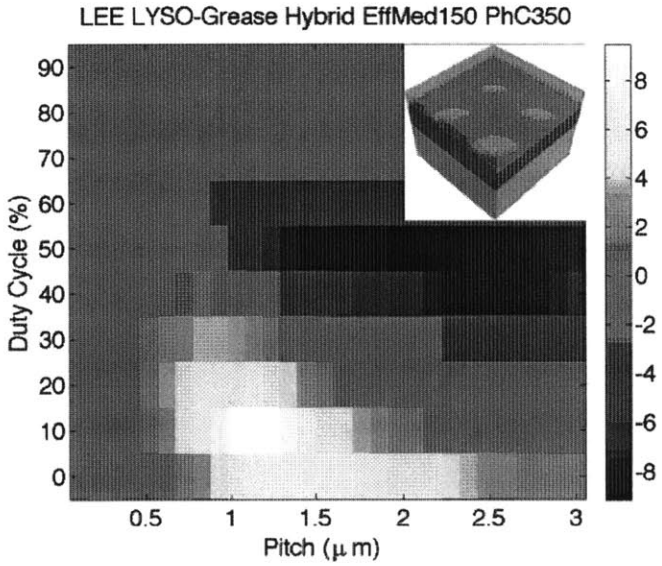

Figure 2-6: Optimum of cone-topping case from the stack thickness 350nm and 150nm for photonic crystal and nanocone, respectively.

photonic crystal. After collecting all these optima, all efficiencies were depicted as shown in Figure 2-7 by their thickness compared to the Air/LYSO and Grease/LYSO interface, respectively. Furthermore, imprinting the hybrid structure is also one alternative, which is also simulated using the same process as shown in Figure 2-8. The available material ACW (AC L2061-B, Addison Clear Wave Inc.) for nano imprint with refractive index at 1.67. In this case, we can have an additional polymer 311RM (MINS-311RM, Minuta Technology) that has the similar index of refraction at 1.52 as a buffer. This additional polymer also could be a good attachment between ACW and the fused silica substrate with index also at 1.5. The material property and imprint process will be discussed in the fabrication section.

As a result, we can choose the best parameters with compromise between the optical performance and fabrication feasibility to apply our structure on scintillator. Results show that the best design is the cone-topping case, and this is because it keeps the completeness of the photonic crystal for diffraction. The diffracted light from the crystal has good impedance matching from nanocones on top of the crystal. The cone-valley case has the worst results that support this argument. A careful proof could be obtained by analyzing the diffraction efficiency of each order using S4.

2.3 Fabrication

The fabrication of a hybrid structure using deposited silicon nitride is the motivation of this work because higher index margin for design and less material degradation compared to the polymer film. However, the process also brings additional issues to the final performance such as intrinsic gain loss by microcrack from deposition heating and absorption of silicon nitride due to inferior deposition condition. An imprinted scenario of hybrid structure was considered to be the better candidate for proof of concept eventually. More discussion about detrimental effects for directly processing the film with LYSO scintillator would be demonstrated in alternative message of this section.

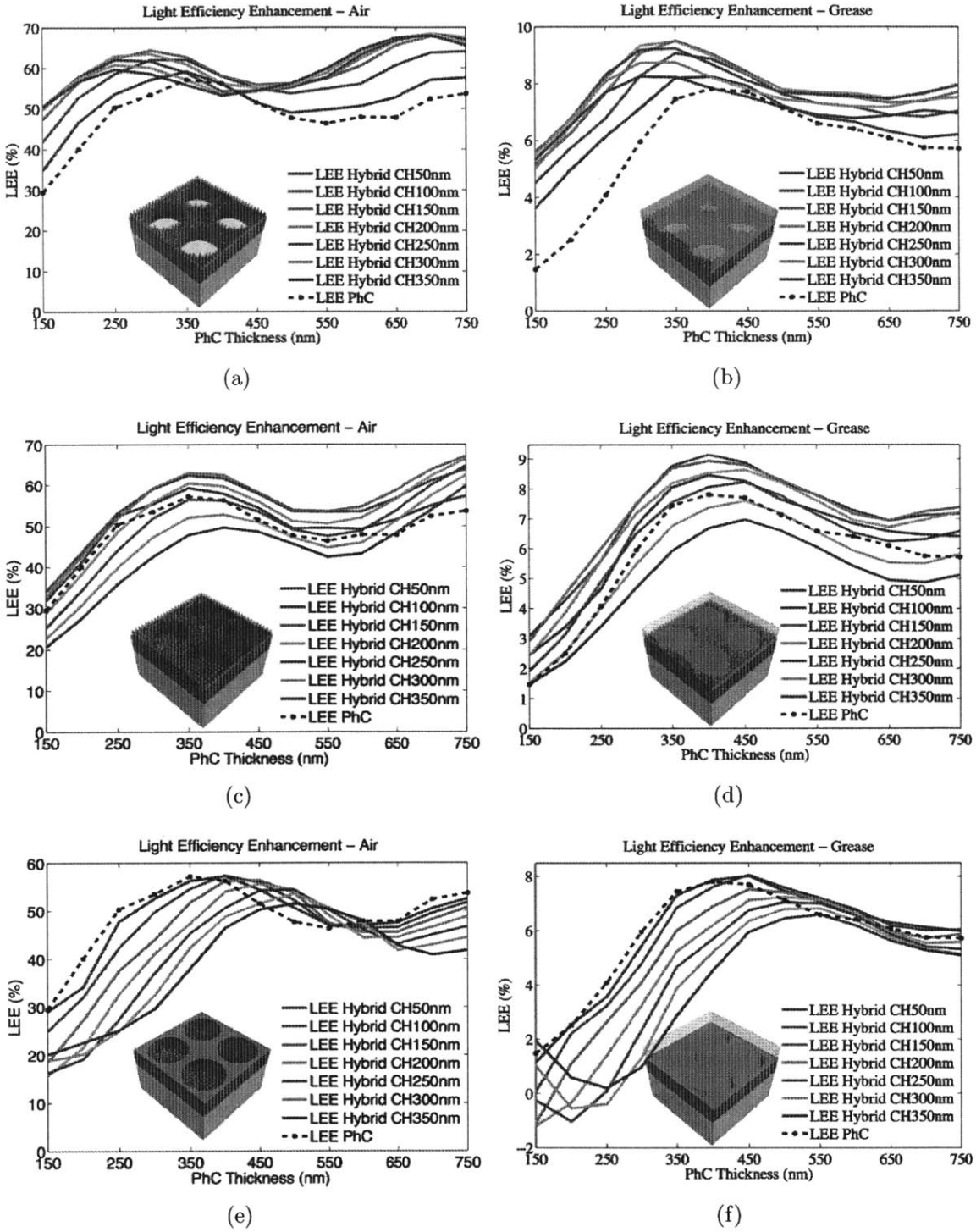

Figure 2-7: Optimization results with air or grease coupling (a) Cone-topping with air (b) Cone-topping with grease (c) Cone-cover with air (d) Cone-cover with grease (e) Cone-valley with air (f) Cone-valley with grease. The performance ranking is Cone-topping > Cone-cover > Cone-Valley.

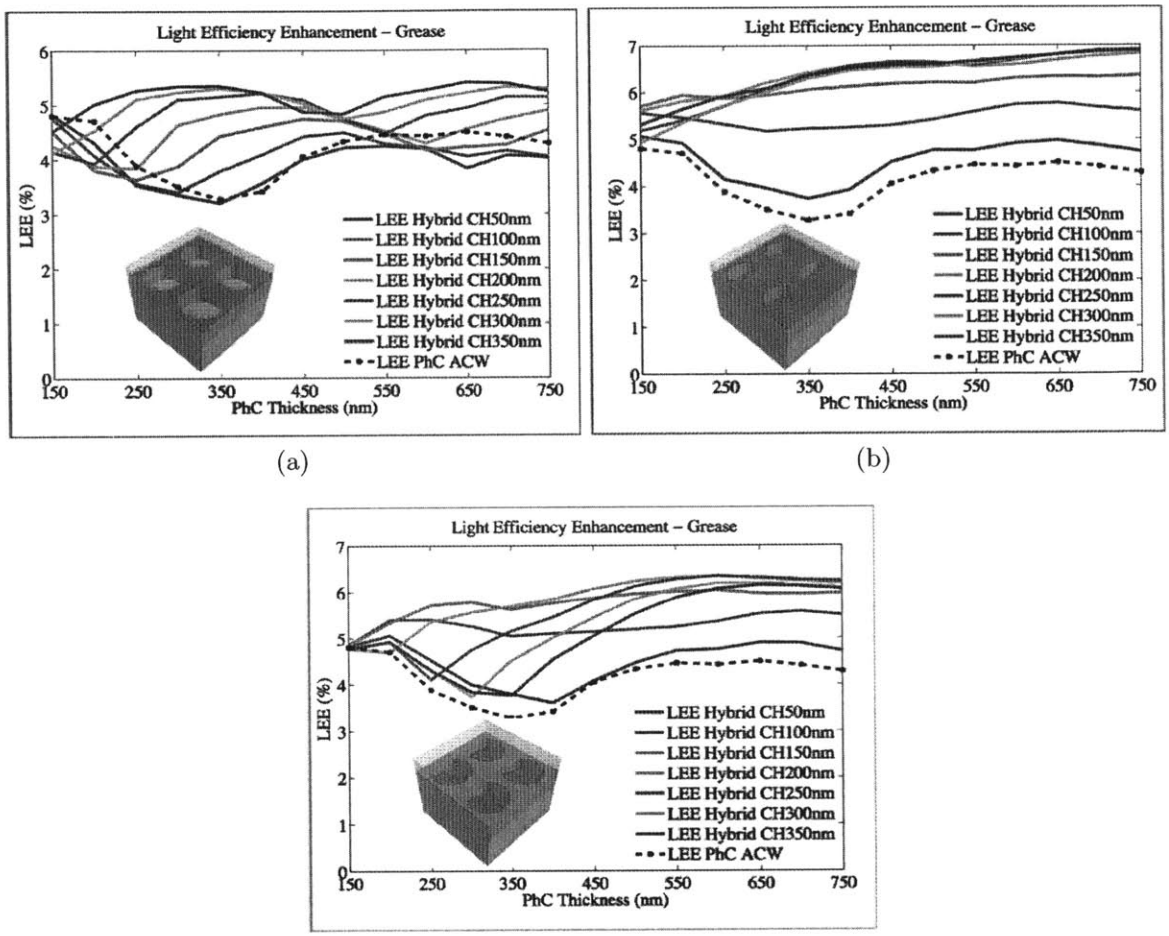

Figure 2-8: Optimization results with grease coupling for ACW polymer (a) Cone-topping (b) Cone-cover (c) Cone-valley.

2.3.1 Process flow

In the previous section, we found the optimum for each case, and the cone-topping hybrid structure yields the best result among three scenarios. Simulation results indicate that parameters for the best efficiency gain at 68.5% consist of 300/700 nm for cone/grating stack. However, this requirement needs a durable hard mask that is hardly achieved in nanosphere lithography available in our lab. Thus, another optimum was needed for fabrication feasibility. Fortunately, another parameter set consisting of 150/300 nm for cone/grating stack with 600 nm periodicity and 10% duty cycle yields an acceptable efficiency gain at 64.5%. However, the LYSO substrate is implicitly not appropriate for directly processing. More details are discussed in

Table 2.2: Parameters for fabrication.

Parameters			
Photonic crystal		Nanocones	
Period	1100 nm	Period	100 nm
Duty Cycle	10%	Thickness	150 nm
Thickness	350 nm		

alternative message section of this chapter. The imprinted hybrid structure is used in the following process. The summary of the chosen parameters were shown in Table 2.2.

The entire process flow is depicted in Figure 2-9. First, a 500nm-thick Si_3N_4 layer was deposited on Si substrate using plasma enhanced chemical vapor deposition

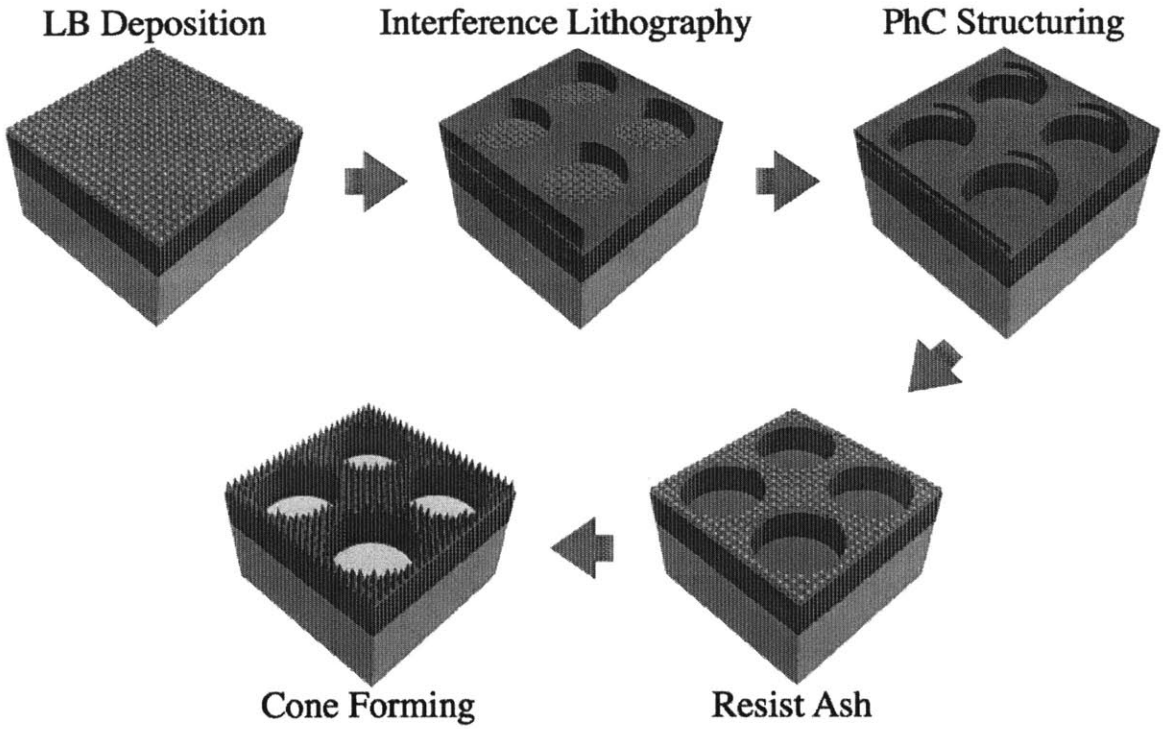

Figure 2-9: Schematics of process flow. 100nm-big beads coating was carried out by Langmuir-Blodgett method. Photonic crystals was defined by Laser interference lithography after ARC and photoresist were spun on. Then sample went through three plasma etching: 15 minutes CF_4 gas for grating patterning, 5 minutes asher for resist removal, and another 5 minutes CF_4 gas for nanocone patterning.

(PECVD) followed by silica beads coating using Langmuir-Blodgett method. The diameter of beads purchased from Fiber Optic Center Inc. is 100 nm and that controls the periodicity of nanocone arrays. Second, the 70nm-thick antireflective coating (ARC, XHRiC-16, Brewer Science Inc.) and 350nm-thick positive-tone photoresist (PFI-88, Sumitomo Chemicals Corp.) for laser interference lithography were spin-coated at 3500 and 900 rpm separately. The sample exposure lasting for 135 seconds in two orthogonal direction was performed by a laser source at 325 nm wavelength using Lloyd's mirror setup to create a 2D gratings. The Si_3N_4 layer was etched by CF_4 plasma for 350 nm in 15 minutes followed by the asher for 5 minutes to remove the residual photoresist and ARC layer. Last, another 5 minutes etching process using CF_4 plasma with the same recipe previously was used to form 150nm-high nanocones on top of the photonic crystal.

2.3.2 Langmuir-Blodgett Deposition

The Langmuir-Blodgett effect was originally used to assemble monolayers or multi-layers of an organic material, deposited from the surface of the liquid by immersing the solid substrate into the liquid. This technique is currently applicable to the nano spheres or particles, which were treated by amphiphilic surfactant with hydrophobic head and hydrophilic tails. In this work, the silica beads with amphiphilic treatment were prepared and dispersed in methanol as solvent. Details about the treatment process are presented in Appendix B. The colloidal solution that is lighter than water

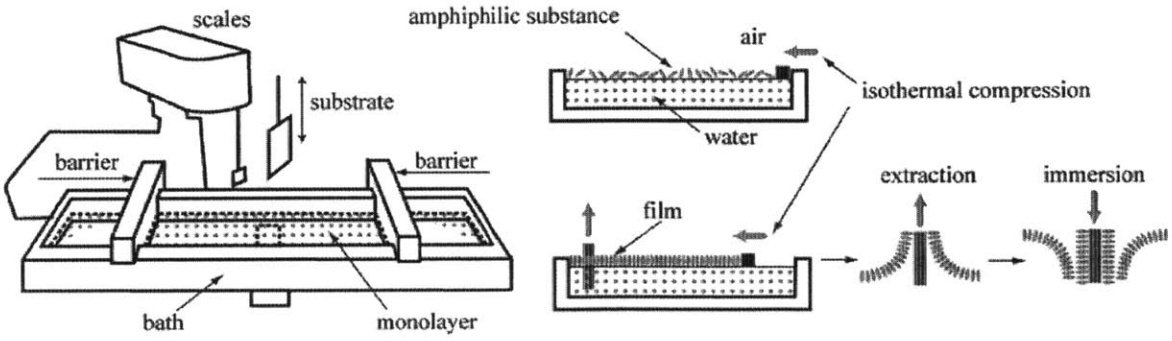

Figure 2-10: Working principle of the Langmuir-Blodgett trough. The compression bar can move isothermally to assemble the monolayer from floating beads [2].

was gently injected into a water-filled Langmuir-Blodgett trough (KSV NIMA 312, Biolin Scientific Inc.) by a injection pump to control the injection rate. Because of the function of hydrophobic head, beads can float on the surface of the water after methanol evaporating out from water as shown in Figure 2-10. After injecting sufficient concentration on the water, the compression bar started to push the floating beads toward the dipping area. At the same time, the surface tension was monitored by a sensor, called Wilhelmy plate, to monitor the surface tension change. The Wilhelmy plate is a thin paper that can be pulled down by the liquid tension as shown in Figure 2-11(a). The surface tension is simply calculated by the Wilhelmy equation as:

$$\gamma = \frac{F}{l \cos\theta} \tag{2.4}$$

where F indicates pull-down force, the l denotes the perimeter of the Wilhelmy plate, *i.e.* $2(w+d)$ as shown in Fig.2-11(a), and θ is the wetting angle between the Wilhelmy paper and water. The most important property of the Langmuir-Blodgett deposition is the surface pressure, which the surface tension was reduced by the bead assembly over the water surface:

$$\Pi = \gamma_0 - \gamma \tag{2.5}$$

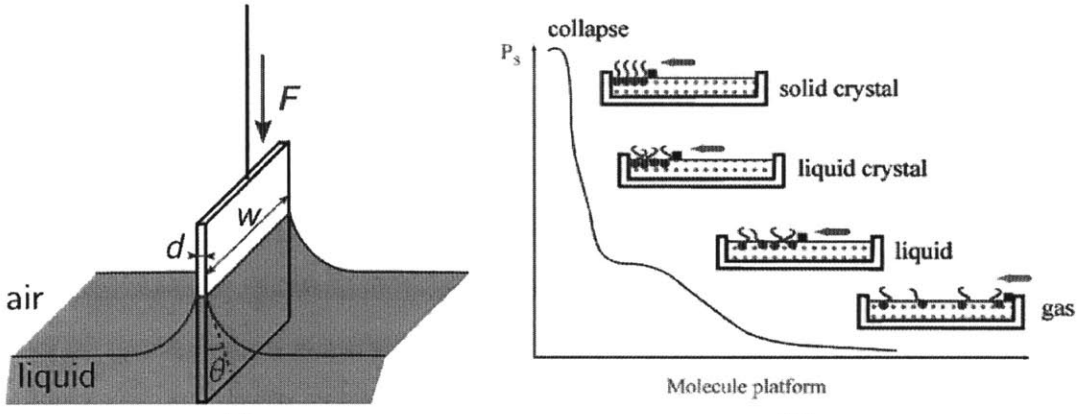

Figure 2-11: Langmuir-Blodgett method (a) Sensing principle of the Wilhelmy plate [3]. (b) Three phases of monolayer: gas, liquid, and solid function of the surface pressure [2].

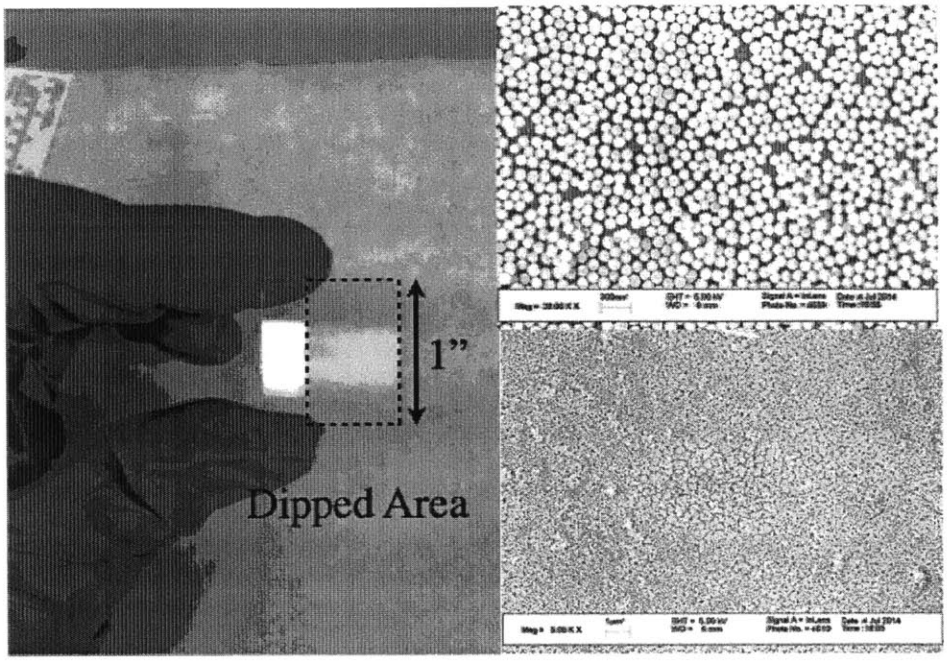

Figure 2-12: Results from Langmuir-Blodgett deposition on the glass slide. Photograph at the left show blue reflection at coating area around 1" x 1". SEM indicates the a monolayer assembled on the glass slide.

where Π is the surface pressure from the surface tension difference between the clean and bead-covered water surface, γ_0 and γ represent the surface tension of water from clean and bead-covered water surface, respectively.

The assembly condition of beads over the water surface is monitored by the surface pressure, and it consists of three phases: gas (dilute), liquid (dense), and solid (compact) as shown in Figure 2-11(b). The best Π is related to the coating material, and should be characterized by the experiment. In this work, the successful monolayer assembly happened at $\Pi = 15$ mN/m, which is controlled by compression bar to ensure assembly quality during dipping and extraction of the sample. Results as shown in Figure 2-12 showed an even coating on the glass slide, which the area with uniform blue reflection at the coating area was seen in the photograph. The micrograph taken by the secondary electron microscopy at different magnifications also showed an uniform beads assembly agreed with observation by naked eye. In addition, the etching test on Si_3N_4 using silica beads as hard mask was also carried out as shown in Figure 2-13. Etching results indicated that 100nm-big beads can only form the 150nm-tall

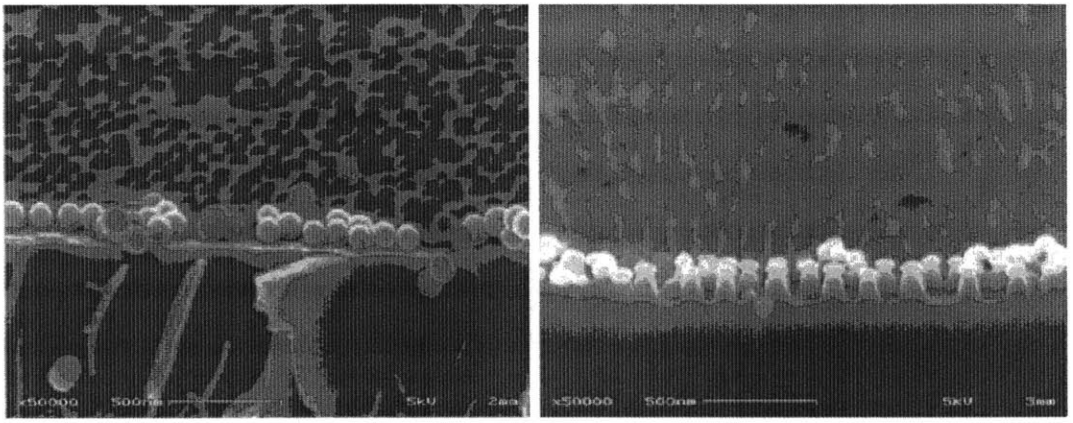

(a) (b)

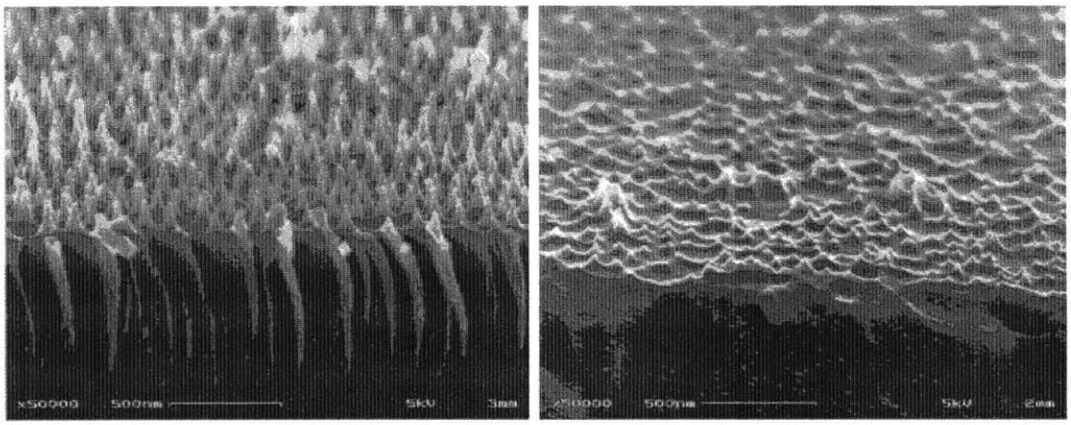

(c) (d)

Figure 2-13: Etching test of Si_3N_4 using silca beads as hard etching mask for (a) 0 (refrence) (b) 2.5 (c) 5 (d) 10 minutes in CF_4 plasma.

nanocone structure after etched for 5 minutes. The structure began to shrink after 5 minutes in CF_4 plasma, which confirmed that taller nanocones were hardly made by nanosphere lithography. Changing to this alternative design was correct decision as expectation.

2.3.3 Laser interference lithography

Optical lithography has dominated the manufacturing of semiconductor industry over decades because patterning defines the design and capacity of the electronic device. Precise positioning and high throughput are always the goal pursued by researchers and engineers. Optical lithography is the mainstream with aforementioned benefits

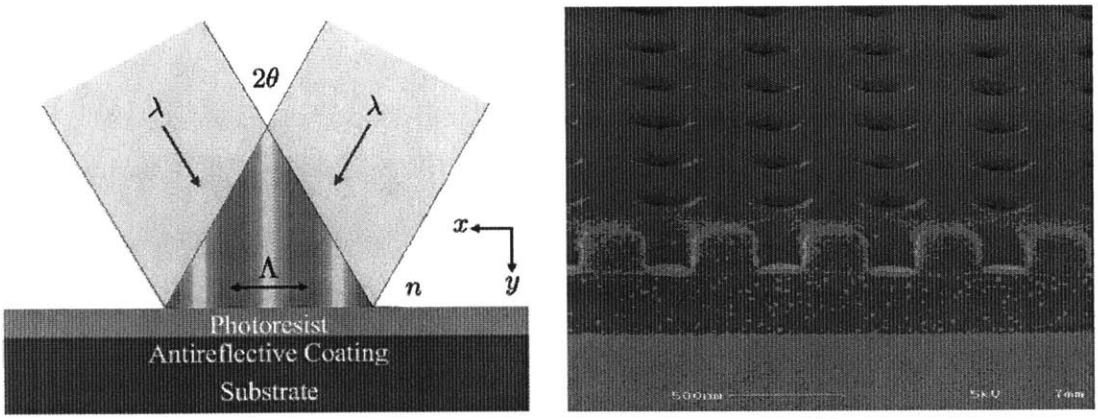

(a) (b)

Figure 2-14: Laser interference lithography (a) Principle of the laser interference lithography. The two beam coming from left and right interfered mutually to form the periodic fringes. (b) An example of exposure results using Lloyd's mirror. SEM showed the photoresist pattern with ARC layer underneath after development.

compared to other nano-lithography techniques such as direct e-beam writing and nanoimprint. Interference lithography is a sort of popular candidate in optical lithography because of the parallel exposure over a larger area within a relatively shorter time, if the periodic pattern was used for the design. Hence, interference lithography was chosen to pattern the photonic crystal over the extraction plane of the scintillator. Laser interference lithography that utilizes a coherent laser light as illumination source defines interference fringes by two mutually coherent plane waves as shown in Figure 2-14(a). The periodicity of the fringes is determined by the intensity pattern as:

$$I = |\vec{E}_L + \vec{E}_R|^2 \tag{2.6}$$

where the $\vec{E}_L$ and $\vec{E}_R$ were the field of coherent laser beams coming from the left and right, respectively. Fields can be expressed as [25]

$$\begin{aligned} \vec{E}_L &= \hat{e}_L A_L \exp\left(-nkx\sin\theta + nky\cos\theta\right)\exp\left(-j\omega t\right) \\ \vec{E}_R &= \hat{e}_R A_R \exp\left(nkx\sin\theta + nky\cos\theta\right)\exp\left(-j\omega t\right) \end{aligned} \tag{2.7}$$

where $\hat{e}_L$ and $\hat{e}_R$ are unit vectors denoting the polarization, and A_L and A_R are the amplitudes of the left and right beams, respectively, $\omega = 2\pi f$ is the optical frequency,

n is the refractive index of the surrounding medium, and $k = 2\pi/\lambda$ is the wave vector. The intensity distribution along the x-direction is then given by

$$I(x) = A_L^2 + A_R^2 + 2A_L A_R(\hat{e}_L \cdot \hat{e}_R)\cos(2nk\sin\theta x) \tag{2.8}$$

The period Λ of the intensity pattern is given by

$$\Lambda = \frac{\lambda}{2n\sin\theta} \tag{2.9}$$

From Eqn.(2.9), the period is fundamentally governed by the wavelength of the interfering beam with the smallest attainable period $\lambda/2n$. An exposure example on photoresist as shown in Figure 2-14(b) showed a 2D hole array on a silicon substrate. The ARC layer in between the substrate and photoresist was used to prevent the scallop sidewall from the resist caused by the interference from the reflected beam. In terms of the implementation of the laser interference lithography, the setup can simply be carried out by placing a mirror with adjustable angle next to the sample to create two beam illumination, which is referred to as "Lloyd's mirror". In short, laser interference lithography is an efficient choice to fabricate the large-area 2D photonic crystal on either the LYSO or Si substrate.

2.3.4 Patterning results and Nanoimprint

Fabrication results were shown in Figure 2-15 corresponding to the proposed process flow in Fig. 2-9. First, the bead assembly on Si_3N_4 film was carried out by Langmuir-Blodgett method followed by Laser interference lithography. After development, the scallop sidewall on photoresist happened due to the thickness of the ARC is constrained by the nanosphere layer instead of the desirable value during the spin-coating. However, it did not affect the following RIE etching in CF_4 plasma to pattern the photonic crystal. The sidewall after the first RIE etching process was still smooth as expectation. Finally, the residual photoresist and ARC were removed by asher, and nanocones formed on top of the photonic crystal by RIE etching again.

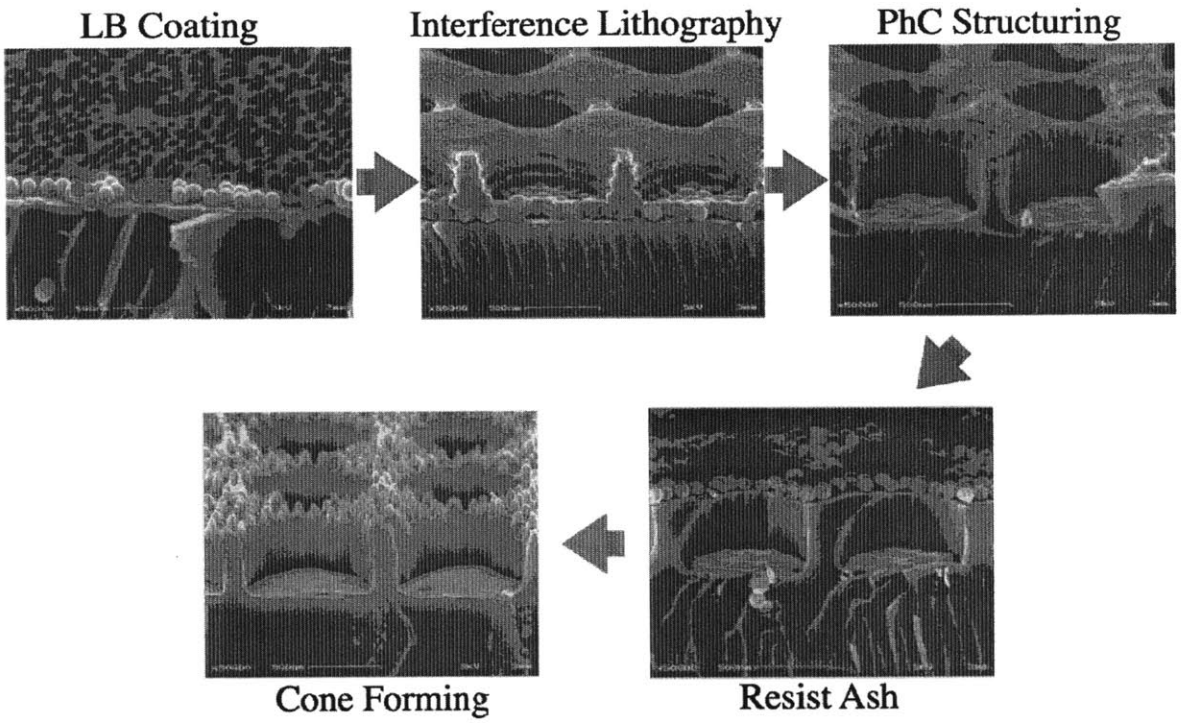

Figure 2-15: Fabrication results were shown by a series of SEM. First, the bead assembly on Si_3N_4 film was carried out by Langmuir-Blodgett method followed by Laser interference lithography. Scallop sidewall on photoresist happened due to the thickness of the ARC is constrained by beads layer instead of the desirable value, but it did not affect the following RIE etching in CF_4 plasma to pattern the photonic crystal. Finally, the residual photoresist and ARC were removed by asher, and nanocones formed on top of the photonic crystal.

Even though direct fabricating the film on LYSO crystal will result in intrinsic gain reduction due to several issues, the fabricated nitride film still can be used as the mold for imprinting the hybrid structure on polymers. The device for final characterization is currently modified as shown in Figure 2-16(a). The 311RM liquid (MINS-311RM, Minuta Technology Co.) with refractive index of 1.52 at wavelength of 420 nm was poured on the as-fabricated mold followed by the covering of fused silica. A careful drop-down of the fuse silica piece could stop the bubble generation. The 311RM as shown in Figure 2-16(b) was exposed by the UV light with the wavelength of 365 nm for 60 sec for curing. After curing, the master mold was separated from the fused silica for the next imprint. Another liquid ACW polymer (AC L2061-B, Addison Clear Wave Coating Inc.) refractive index of 1.52 at wavelength of 420 nm as shown

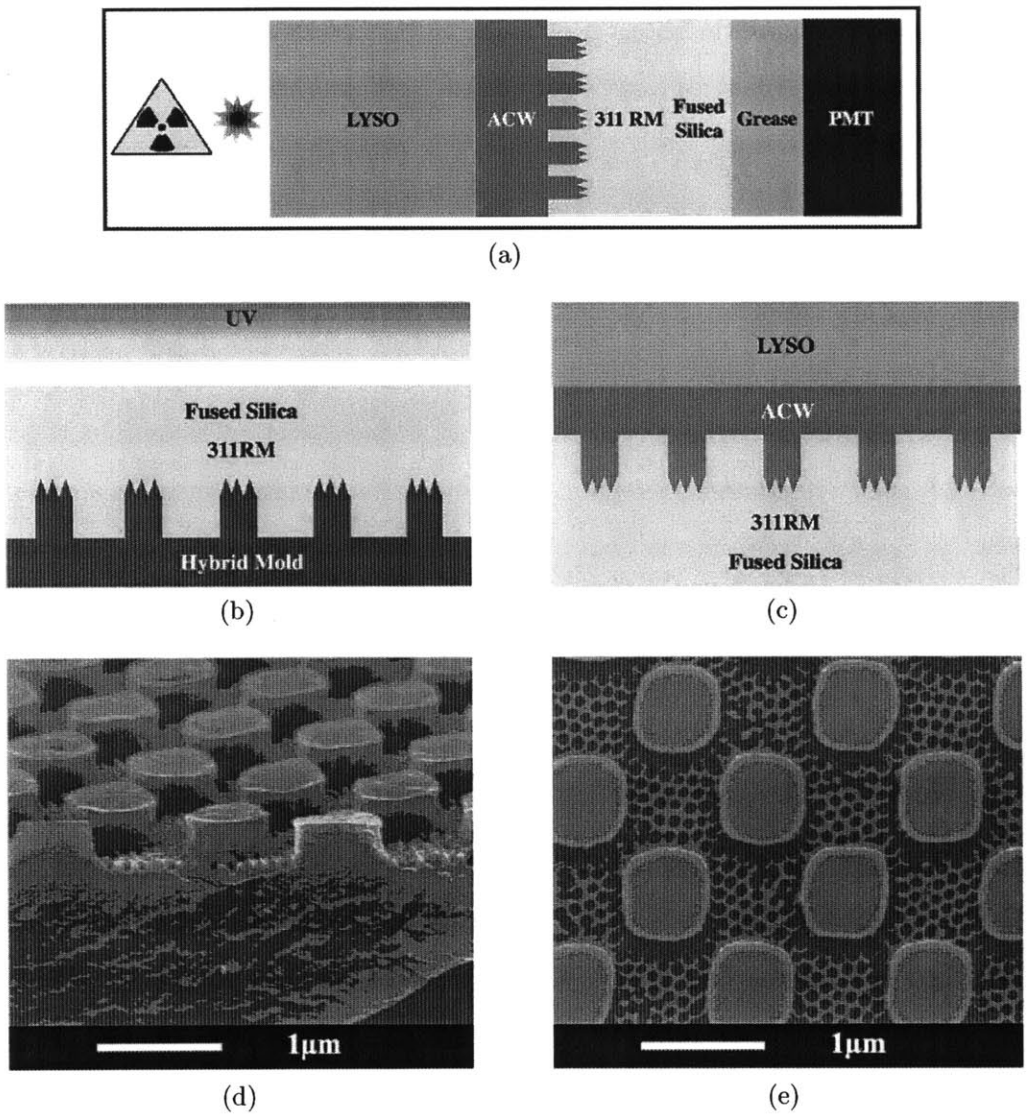

Figure 2-16: Characterization of the imprinted hybrid structure (a) Configuration. Hybrid structure fabricated on ACW polymer by the counterpart 311RM on the fused silica imprinted from the silicon nitride mold. (b) 311RM curing by UV after filling up the gap between the Si_3N_4 mold and fused silica. (c) The curing process of ACW polymer also uses the UV light with LYSO stamping. (d) and (e) both shows the imprinted results of 311RM polymer from cross-section and top-view, respectively. Imprinted 311RM becomes the counterpart of ACW that the main structure used for efficiency enhancement.

in Figure 2-16(c) was poured on the counterpart made from 311RM, and then the LYSO crystal was pushed toward ACW layer followed by the exposure of 365 nm UV light for 3 mins. The imprint result on 311RM polymer as shown in Figure 2-16(d) and (e) indicates the inverted structure from the master mold, and the ACW polymer

filled in later could be exactly the same of the duplication of that in master mold. After imprint process, the materials are bounded together for characterization. The exit of the device now becomes the fused silica whose index is 1.46 at the wavelength of 420 nm. In addition, the LYSO could be detached from the film manually without breaking itself. After cleaning by Isopropyl alcohol, the LYSO crystal could be reused for another imprint process.

2.4 Characterization

2.4.1 Principle of scintillation detector

Understanding the working principle of the PhotoMultiplier Tube (PMT) is the first step of characterization. High energy particles or rays convert their energy to non-ionizing photons via scintillator. These non-ionizing photons that pass through the PMT window are converted to photo-electron by the photocathode as show in Figure 2-17. A focusing electrode that accelerates photoelectrons to hit the first dynode generate secondary electrons. The total number of secondary electrons were amplified by repeating the same collision on dynode for several times until all electrons are collected by anode. The anode connected to a charge amplifier transfers the total counting number of charges to a voltage output, which is a feed for a Analog-to-Digital Converter (ADC) in the MultiChannel Analyzer (MCA) for final data translation. The channel number representing the pulse intensity is linearly proportional to the photon number from the photocathode within a clock time. The final output on computer showed that counts are distributed over different channel numbers. This process may be expressed by:

$$N_{ch} = \frac{2^{10}}{V_{\mathrm{ADC,max}}} \eta_{\mathrm{amp}}\, \eta_{\mathrm{PMT}}\, N_{\mathrm{ph,sc}} \propto N_{\mathrm{ph,sc}} \tag{2.10}$$

where N_{ch}, $N_{\mathrm{ph,sc}}$, η_{PMT}, η_{amp}, and $V_{\mathrm{ADC,max}}$ represent the channel number output from MCA, the extracted photon number from the scintillator, the gain of PMT, the gain of charge amplifier, and the maximal supply voltage to MCA. Therefore,

the peak on the histogram from MCA determined the strongest pulse converted by this scintillator-PMT set. The light gain from hybrid structure can be investigated through the increase of the channel number peak, *i.e.* a brighter or darker signal output, after using the hybrid structure to extract the light.

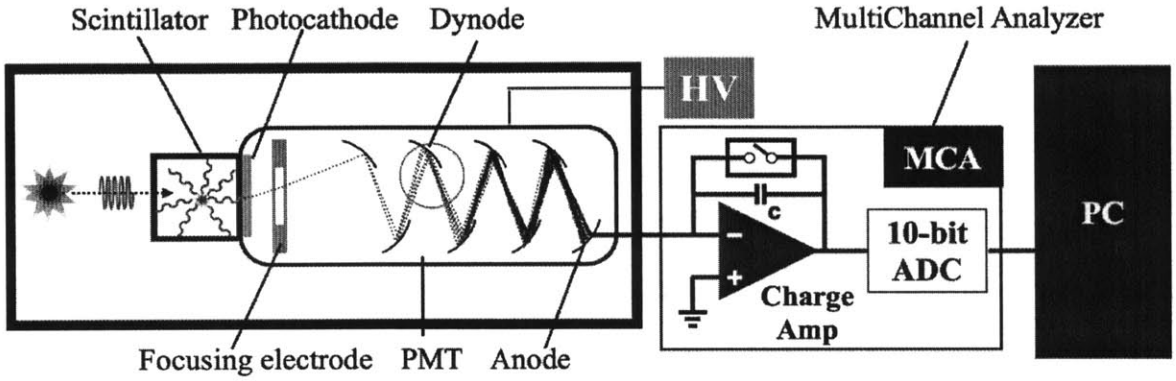

Figure 2-17: Operating principle of PhotoMultiplier Tube (PMT). PMT converts the visible light to photoelectrons using photocathode, and photoelectrons were amplified by several dynodes. Secondary electrons from dynodes were collected by the anode and counted by the charge amplifier. The output voltage from the charge amplifier was numbered by analog-to-digital converter (ADC) for final output data. Therefore, the channel number at multichannel analyzer (MCA) is proportional to the number of photoelectrons.

2.4.2 Measurement results

The LYSO scintillator with hybrid structure was characterized with the aforementioned PMT setup using Co-57 as excitation source, whose emission peak at 122 keV (low energy gamma-rays). The gamma-ray generated from the decay of the atomic nuclei will follow the interaction as described in the first section of the this chapter. The signal of secondary electrons collected by PMT (R6233-100 Bialkali, Hamamatsu) with 650 high voltage was amplified by a charge amplifier (Model 113, ORTEC) for a voltage output. This voltage output will correspond to a certain level of 10 V that is digitalized by a 10-bit MCA (MCA 8000D, Amptek). In the sample placement, the extraction plane of the scintillator faced toward PMT glass window with optical grease in between for index matching. The scintillator was entirely masked by the black plastic cover of the PMT with teflon wrapping. The result as shown in Fig. 2-18

reveals a 4.05% light gain using the imprinted configuration of the hybrid structure. The spectrum .

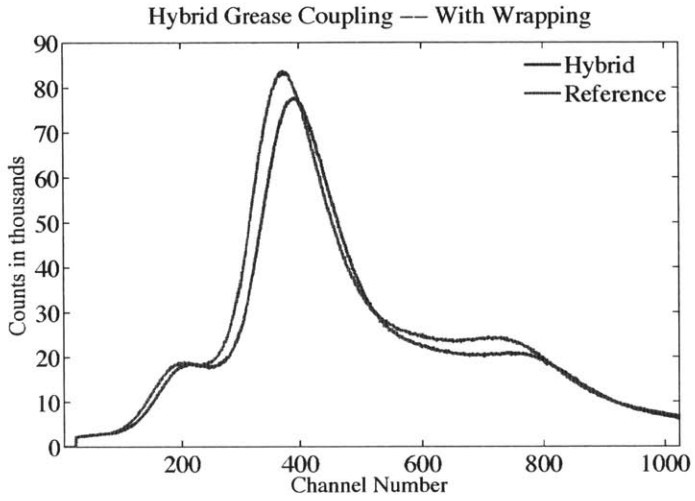

Figure 2-18: Light gain measurement. The peak of the channel number shifts to the right from 378.1 to 395.4 after using the imprinted configuration of the hybrid structure with the same scintillator.

2.4.3 Discussion

Direct processing silicon nitride film on LYSO results in problems such as micro cracks and absorption, which both decrease the light gain. Because of narrow gain margin with and without the structure, it is unable to compensate the drop in intrinsic gain even with structure. Thus, imprinted hybrid structure becomes the alternative for implementation. Here, we demonstrate the measured gain loss from heating and absorption from the deposited film as shown in Figure 2-19. The reference sample are both newly purchased from the vendor without any process. In Figure 2-19(a), the sample was heated up to 250° with the same temperature and time duration of PECVD process. The channel number drops by 4.44% when measuring the extraction efficiency with teflon wrapping and grease coupling. The root cause of the efficiency drop is not clear yet. The reasonable explanation of this phenomenon is that the generation of micro cracks after heating the LYSO substrate. No literature measuring the thermal expansion of LYSO was found, but the used LYSO substrate was cracked

after heating up for several times. This indicates the uneven thermal expansion of LYSO crystal during annealing.

Another issue results from the quality of Si_3N_4 film by PECVD. In general, the pure Si_3N_4 is transparent at the wavelength of 420 nm, but the film from PECVD could change its composition to be SiN_x that cause different optical constants including index of refraction and extinction coefficient. Some research indicates that SiN_x could have higher index along with increasing the extinction coefficient by the absorption from SiN_x:H bond [26]. Hence, the ratio of the flow rate between the NH_3 and SiH_4 species should be investigated for the best non-absorptive SiN_x film.

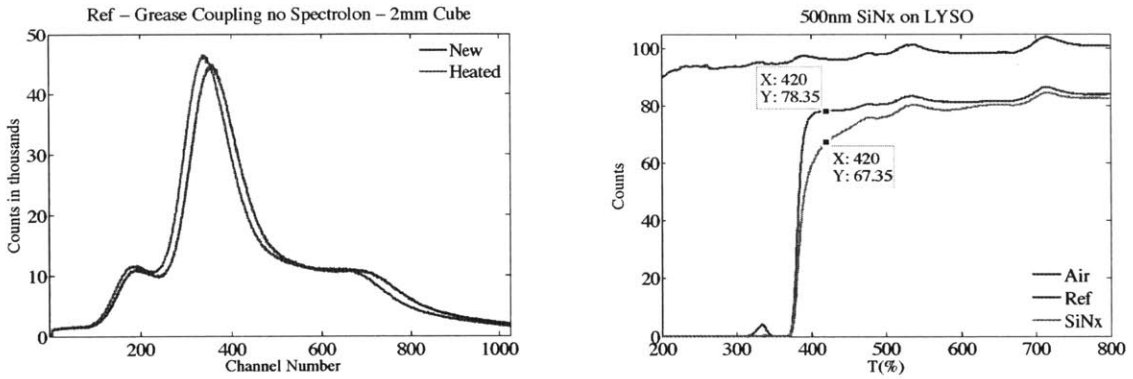

(a) (b)

Figure 2-19: Intrinsic gain drop due to processes (a) Extraction loss by sample heating. The same annealing process as well as the deposition causes the extraction efficiency of the same LYSO crystal drop by 4.44% (b) Absorption of silicon nitride film. A 11% transmission loss observed at the wavelength of 420 nm on the same crystal with and without Si_3N_4 coating indicates that the film quality should be tuned by controlling disposition parameters.

2.5 Summary

In order to enhance the light extraction efficiency of the scintillator, a hybrid structure that consists of nanocone array on top of the 2D photonic crystal was designed to yield the highest gain for grease coupling. Structure parameters of the deposited Si_3N_4 film using PECVD were optimized to match the best coupling efficiency. In terms of the fabrication feasibility, the imprinted configuration of hybrid structure

was used for implementation. The corresponding geometry of the hybrid structure is 1100 nm in pitch, 10% duty cycle, and 350 nm in thickness for photonic crystal; 100 nm pitch and 150 nm in thickness for nanocones. Finally, the fabricated LYSO sample was characterized with the PMT to demonstrate a 4.05% efficiency gain that is close to simulated value 3.27%.

THIS PAGE INTENTIONALLY LEFT BLANK

Chapter 3

Implementation of Nanostructured Lüneburg Lens

Contents

3.1 Introduction

In 1944, Rudolf Karl Lüneburg proposed a gradient-index (GRIN) omnidirectional lens that brings a plane wave from an arbitrary incoming direction to a geometrically perfect (*i.e.*, aberration free) albeit still diffraction limited focus at the lens edge [27]. In optical frequencies, exact control of the gradient index to an arbitrary prescription is notoriously difficult to achieve directly. Instead, Lüneburg designs have been proposed and implemented using dispersion, for example from gradient-

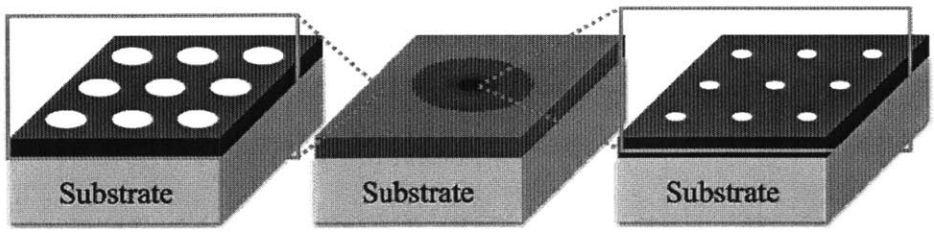

Figure 3-1: The concept of the nanostructured Lüneburg lens consists of an array of nanorods or nanoholes with varying diameter to control the effect index of refraction at each coordinate location.

thickness waveguides and gradient-thickness polymer on metal films at plasmon resonance, to determine an effective gradient index instead as we presented in the chapter 1 [12, 14, 13, 28]. However, the Lüneburg design with gradient-thickness dielectrics has ill confined mode within the device layer, and the intrinsic propagation loss from metal surface is still not comparable with silicon photonics even using the optically pumped polymer gain medium [15]. In addition, neither of them are compatible with current manufacturing of silicon photonics.

My former group member, Satoshi Takahashi, first proposed a nanostructured Lüneburg lens that consists of an array of nanorods with constant periodicity but varying diameters to control the desirable effective index of refraction (EIR) at each grid point as shown in Figure 3-1 [4]. The entire device was built up on a silicon-oxide-insulator (SOI) substrate that is compatible with silicon photonics. At design level, he designed the nanorod array based on two dimensional (2D) assumption, that is, the rod is infinitely thick. This assumption strongly conflicted with the real fabrication, which the rod has finite thickness to yield lower EIR than our expectation. The characterization also did not consider the modal dispersion while a multimode waveguide was used at that time as shown in Figure 3-2. Another group fellow, Hanhong Gao, followed this concept but used a three-dimensional (3D) model to fix the imperfection of 2D assumption. Besides computing the EIR of nanorod arrays numericallly, he also solved the dispersion relation for the EIR of nano rod arrays by an all-analytic approach with shorter computation duration [29]. In this approach, he replaced the nanorods with a continuum of a certain effective permittivity $\varepsilon_{\text{eff}}^{\text{2D}}$ [30, 31]. He also calculated the $\varepsilon_{\text{eff}}^{\text{2D}}$ from 2D lattice of infinite-height holes using

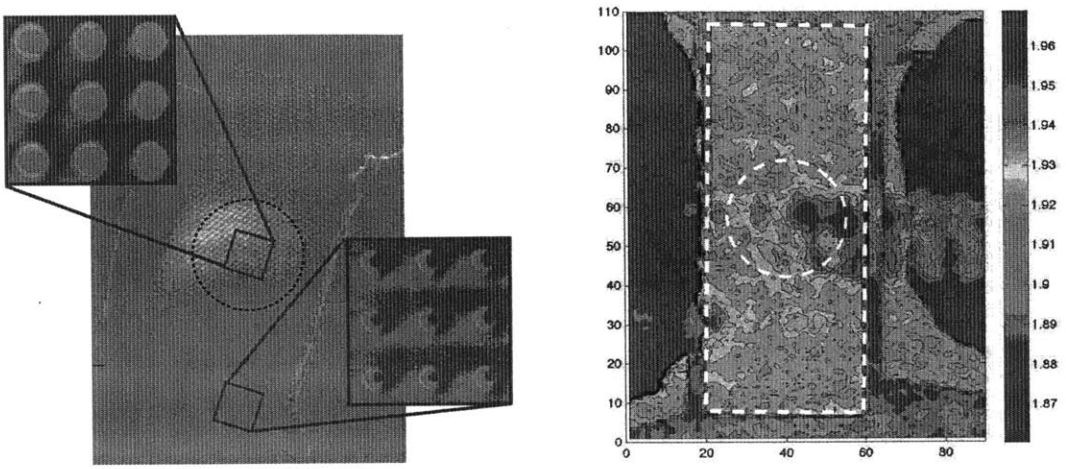

(a) (b)

Figure 3-2: Previous results of the nanostructued Lüneburg lens devised using nano rod array based on the 2D assumption (1) Secondary electron micrograph of the device (2) Characterization by near-field scanning optical microscopy. Note that the intensity contrast between focal spot and other places was only 0.05 [4].

second-order effective medium theory, and substituted $\varepsilon_{\text{eff}}^{\text{2D}}$ back as the permittivity of a slab with finite thickness, sandwiched between semi-infinite spaces of air above and SiO_2 below. The EIR could be found under the weakly guiding approximation by solving the waveguide dispersion relationship. This method as shown in Figure 3-3 was referred as Effective Guiding Medium (EGM), which is distinct from Direct Band Diagram (DBD) [32].

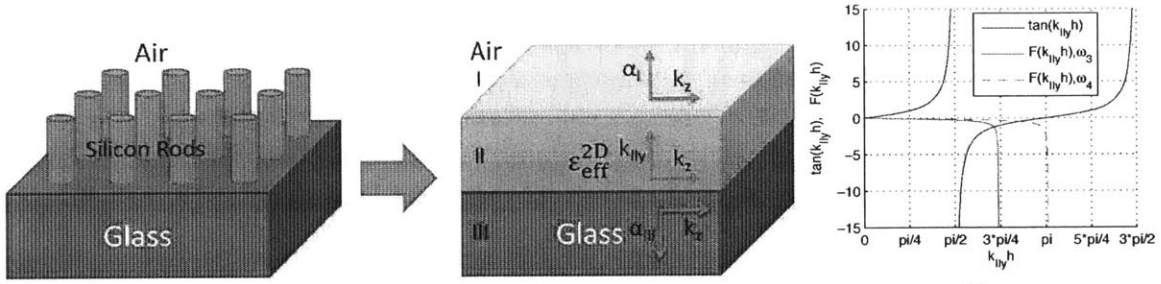

(a) (b)

Figure 3-3: Nanostructued Lüneburg lens using nanorod arrays (a) Effective guiding medium (EGM) approximation of 2D finite height rod lattice structure (b) Graphical solutions of wave guidance condition for transverse-magnetic polarization. Blue and red lines are the left and right hand sides of these equations, respectively.

In this chapter, I am going to present a more practical design of nanostructured Lüneburg lens based on the aforementioned background. Moreover, I fabricated the Lüneburg lens with consideration of entire device for characterization using nanohole and nanorod arrays, respectively. The challenge of structure patterning was on nanorod side that required the Proximity Effect Correction (PEC) for e-beam lithography due to the higher dose and the tiny gap between structures. The modal analysis for the coupling waveguide and the transmission of all components were also studied to ensure that the power arrived at the lens region is enough for measurement. The characterization was facilitated by Near-field Scanning Optical Microscopy (NSOM) but with better control capability and light coupling interface compared to that in other works. The post-analysis of the NSOM image was proceeded by Finite Difference Time Domain (FDTD) software to compare with NSOM results. Finally, an intuitive interpretation of wave behavior of nanostructured Lüneburg lens using Wigner Distribution Function (WDF) and Hamiltonian ray-tracing was offered at the end of this chapter.

3.2 Design and Simulation

3.2.1 Effective Index of Refraction of the Photonic Slab

Although Hanhong Gao had developed a faster EIR solver based on effective medium theory suing EGM method, the mode of the structure can not be computed simultaneously from the solver. In addition, the nanostructured Lüneburg lens also requires an impractical amount of FDTD simulation. Therefore, I used MIT Photonic Band (MPB) mode solver along with a MIT Electromagnetic Equation Propagation (MEEP) FDTD software, which both freeware are developed in MIT AbInitio research group [33, 34]. They not only offer cross-functionality between each other, but also use the same storage format of HDF5 that could be read by MATLAB for data post-processing. Here we presented an example of dispersion for periodic rod and hole arrays with the same diameter as half of the period as shown in Figure 3-4. The

EIR is given by:

$$n_{\text{eff}} = \frac{c\beta}{\omega} \tag{3.1}$$

where n_{eff} denotes the EIR, β means the propagation constant, and ω represents the desirable frequency. By computing the dispersion for rods and holes at different diameter, we can create a library of EIR as function of the structure diameter. This library can be generally combined with desirable refraction index distribution to generate a design layout.

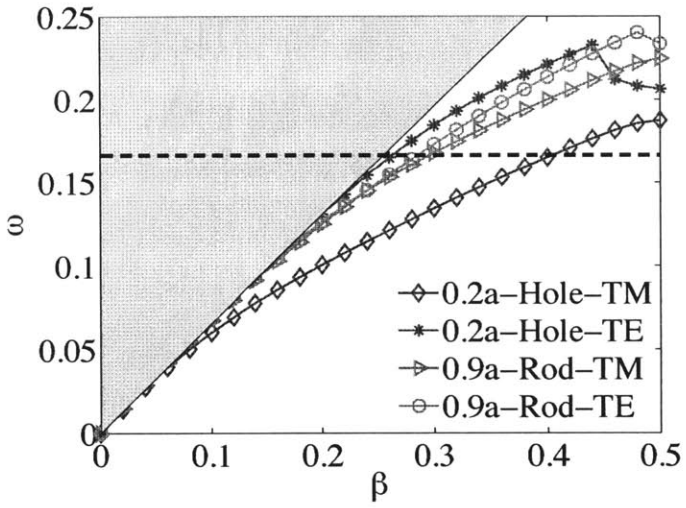

Figure 3-4: Fundamental mode of the dispersion diagram for TE-like and TM-like polarization in 3D rod and hole structures. The nominal diameter of rods and holes are $0.2a$ and $0.9a$, respectively. The grey patch denotes region of "leaky mode" defined by SiO_2 light line, and the black dotted line marks the desirable frequency.

3.2.2 Design Parameters and Structure Specifications

The MPB computation is carried out along with periodic boundary condition by default, so the cell used for simulation normally will be chosen much larger than the dimension of the existing mode distribution in case of the interference from adjacent cells. Usually, this cell is called "supercell" in a 3D simulation. The nanostructured Lüneburg lens is constructed on the SOI substrate compatible with silicon photonics, so the supercell for computing the dispersion diagram is set as shown in Figure 3-5. In the EIR computation, the asymmetric waveguide is used in this work by choice, and

all dimensions used in MPB computation are normalized to the lattice constant a, *i.e.* one-sixth of the desirable wavelength (258.3 nm), as we used in our paper [29]. The height of the air and SiO_2 layer are the same as $10a$ (2.58 μm), and the device layer is 320 nm. Computation results for both rod and hole cases as shown in Figure 3-6 will be used later to construct the design layout for the verification and fabrication.

In Figure 3-6(a), the nanorod array offers much milder index variation for the requirement of Lüneburg lens operated in TE-like polarization, and the rapid increase of the EIR in TM-like condition is going to be very challenged for the size control of rods during fabrication. On the other hand, only TM-like condition at hole case provides the sufficient index variation for design. In fact, the thickness of 320 nm is going to contain the fundamental TM-like mode anyway. Therefore, this work will focus on TM-like polarization for both rod and hole cases to proceed the fabrication. Take hole-slab design for example. Based on this geometry, the upper limit of EIR for the lens is constrained by the minimum feature size that the fabrication capability allows. We choose upper limit of EIR as 2.4 corresponding to the minimal hole diameter as 90 nm, which is feasible in our e-beam lithography facility. The background index of the lens can be determined as 1.7 using Eqn. (1.2) with upper limit of EIR, and this value is essentially larger than the refractive index of the cladding layer for

MPB Parameter	Value
Wavelength λ	1.55μm
Lattice constant a	λ/6 (258.3nm)
h	320nm
H	10a (2.58μm)

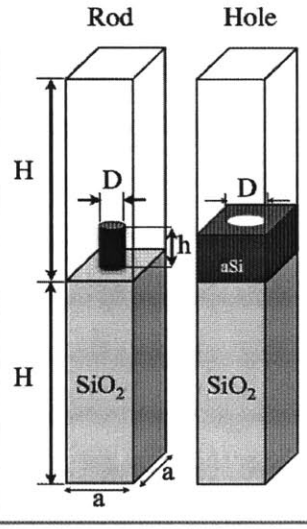

Figure 3-5: All parameters used in MPB for the EIR computation.

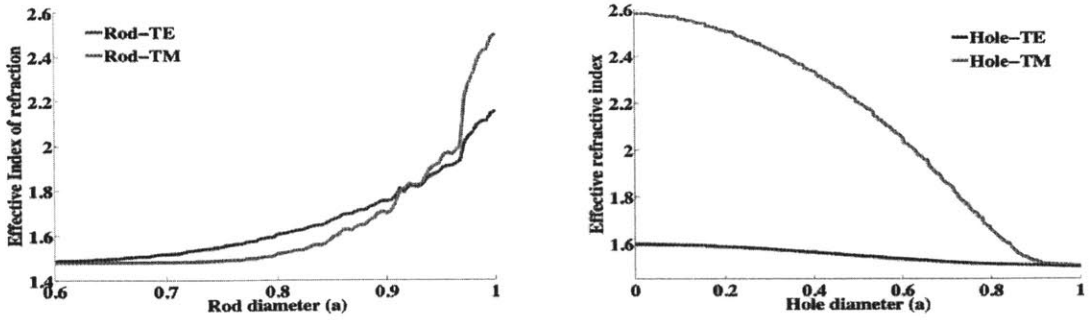

(a) (b)

Figure 3-6: The EIR library for constructing the nanostructured Lüneburg lens in both cases (a) Rod (b) Hole.

satisfying the guiding condition. The index variation of the nanostructured Lüneburg lens is eventually bounded between 1.7 and 2.4. Accordingly, the nanohole diameter will vary from 90 to 203 nm. The same criterion can apply to that in rod case. In summary, all specifications for both cases are listed in Table 3.1.

Table 3.1: Specification summary of the nanostructured Lüneburg lens at TM-like polarization.

Design Specification	Rod	Hole
Period	258.3nm	258.3nm
Structure diameter	214nm < D < 251nm	90nm < D < 203nm
Gap between structure	7.3nm < a-D < 44.3nm	56.3nm < a-D <165.3nm

3.2.3 Simulation

Designs of rod and hole cases for TM-like polarization have been obtained from EIR library, and now we can verify the design with MEEP (FDTD software) to simulate the performance for each case. The schematic of the layout as shown in Figure 3-7 represents the design using hole-slab, but the the same ceoncept can also be applied to rod-slab case, and their performance as shown in Figure 3-8 are both verified using MEEP. The line source at left hand side approximates a plane wave illumination, and the E_z field denoted by the color shading at the background shows the focusing

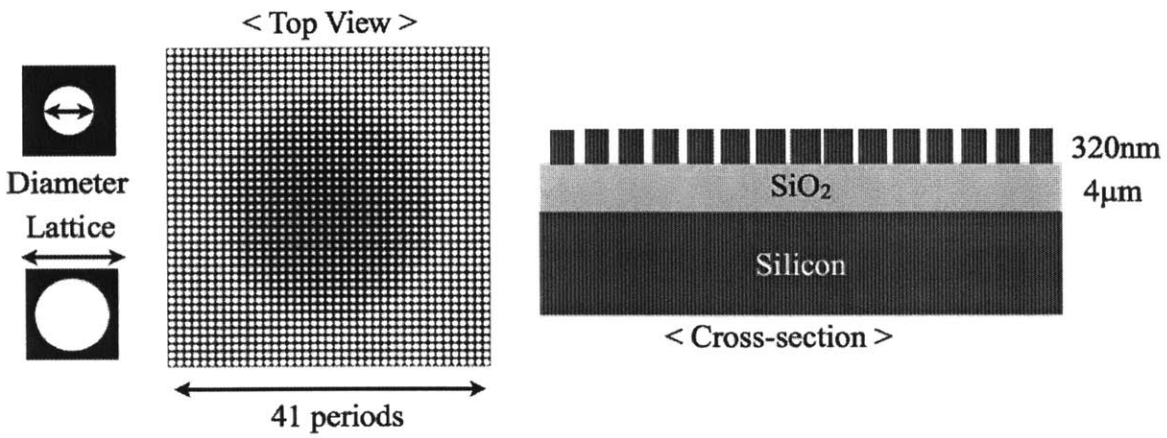

Figure 3-7: Schematics of nanostructured Lüneburg lens constructed by nano hole arrays.

behavior of Lüneburg lens. The structure contour at the background also reveals the design for each case separately.

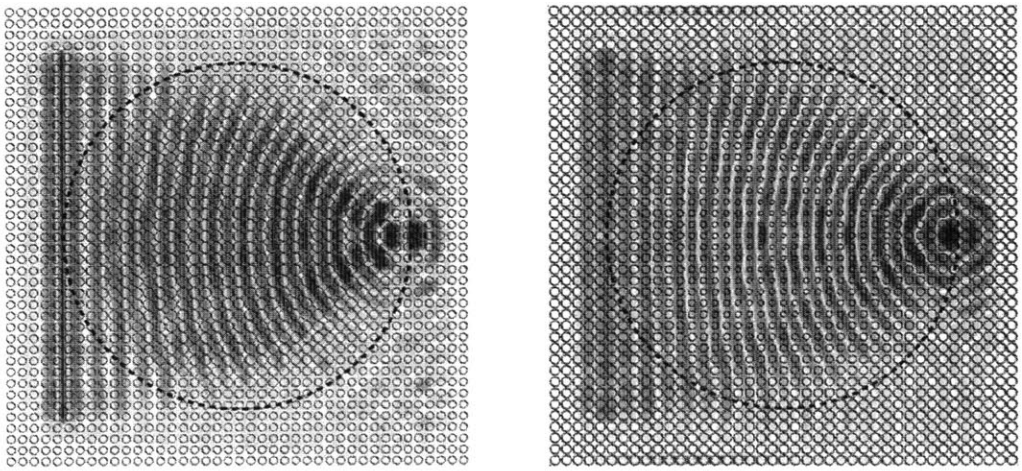

(a) (b)

Figure 3-8: Performance verification using MEEP for (a) Rod-slab lens (b) Hole-slab lens. The black dotted line denotes the lens region, and the color at background overlaid with structure contour represents the E_z field (direction perpendicular to the paper).

3.2.4 Entire Device

After performance check, we next consider characterization before we start the design of the process flow. In order to carry out the characterization, the nanostructured

Lüneburg lens will be embedded into a waveguide as shown in Figure 3-7, and the width of the waveguide is designed as 10.6 μm in order to facilitate the fabrication of the device. However, this width allows multimode propagation, violating the single-mode propagation assumption that was inherent in the EIR calculation. Moreover, if the multimode propagation were allowed, the undesirable effect of bi-foci would ensue [35]. Later in this chapter, there will be more discussion on modal illumination. To secure the single-mode operation, we designed a taper-like feed from a coupling waveguide to the lens region. The entire structure is shown in Figure 3-9. The coupling waveguide is bent with curvature radius of 25 μm to make a 200 μm lateral offset for preventing the stray light of the source fiber coupled into our detector. The mode is slowly evolved and retained by a 300μm-long tapered waveguide from coupling waveguide to lens region after second bending. Another consideration to maintain the integrity of the fundamental mode is the vertical sharpness of the coupling waveguides walls. For this purpose, a durable hard mask for vertical etching of the structure is required.

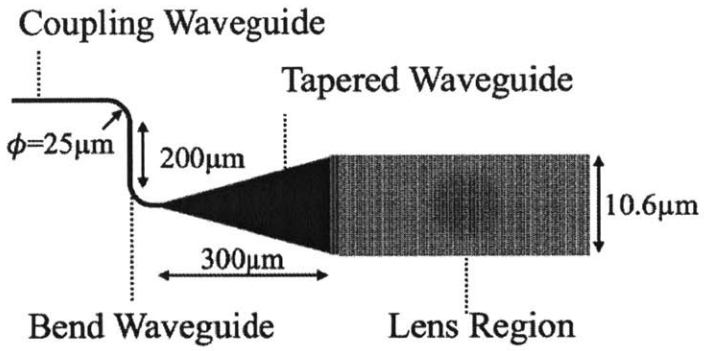

Figure 3-9: Entire design for hole-slab Lüneburg lens. The fundamental mode excitation with TM-like polarization is controlled by the dimension of the coupling waveguide. Bend waveguide prevents the stray light from source fiber interfering with the evanescent wave over the lens region, and the tapered waveguide pertained the mode to lens region.

3.3 Fabrication

3.3.1 Process Flow

In this work, we fabricate our device on the silicon-on-insulator (SOI) substrate made by plasma-enhanced chemical vapor deposition (PECVD). In addition to monocrystalline Si (c-Si), amorphous Si (a-Si) is also a good candidate of the device layer due to comparable index of refraction as well as c-Si, low absorption loss around the wavelength of 1550 nm, and accessible fabrication processes. The entire process flow is depicted in Figure 3-10 for the rod-slab lens. We coat the SOI substrate with spun-on hydrogen silsesquioxane (HSQ, XR1541-006 of Dow Corning) for e-beam lithography (ELS-F125, Elionix). The resist thickness for HSQ is 130 nm under 1000 rpm spin coating. The dose of e-beam writing is 10600 $\mu C/cm^2$ with development by a salt solution consisting of 1 wt% NaOH and 4 wt% NaCl for 60 seconds at 23°C [36], whose the schematic is shown in Figure 3-10a. The salt developer provides the better contrast for HSQ development compared the conventional tetramethylammonium hydroxide (TMAH) developer. Subsequently, the pattern is transferred by reactive ion etching with the gas combination of BCl_3, and Cl_2, and Ar as shown in Figure 3-10(b) for 15 minutes. The key parameters of this RIE process are outlined in Appendix B. Finally, a 10nm-thick Si_3N_4 layer was deposited also by PECVD for eliminating the surface roughness scattering [37]. More details about the challenge in lithography and the proximity effect correction will be discussed in the next section.

In the fabrication of hole-slab lens, the resist was replaced with a positive-tone ZEP-520A resist (1:1 copolymer of α-chloromethacrylate and α-methylstyrene, ZEON) because of saving the exposure time and low dose assignment during exposure to avoid the proximity effect. Furthermore, a different HSQ layer was used in the exposure stack due to better etching selectivity to a-Si in the following etching process. The entire process flow is depicted via Figure 3-11. We coat the SOI substrate with spun-on HSQ (FOX-14 of Dow Corning) as hard mask followed by ZEP-520A resist for e-beam lithography (ELS-F125, Elionix). The stack thicknesses for both HSQ and ZEP-520A are 130 nm under 6000 rpm spin coating. The dose of e-beam writing

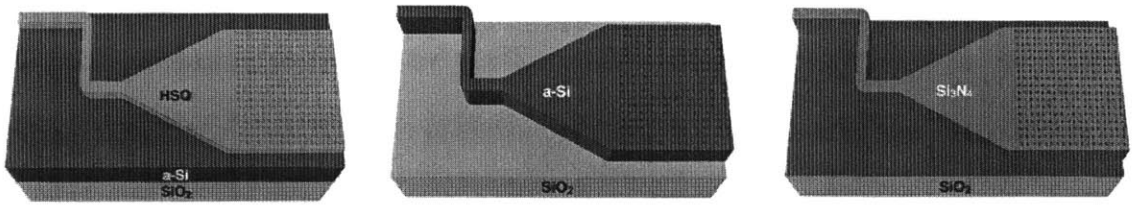

(a) (b) (c)

Figure 3-10: Process flow for rod-slab Lens (a) Pattern the device by e-beam lithography on 6% HSQ (b) Etching device layer by RIE with gas combination of BCl_3, and Cl_2, and Ar (c) Deposition of silicon nitride by PECVD for decreasing surface roughness scattering.

is 300 $\mu C/cm^2$ with development by *o*-xylene (98%, Sigma-Aldrich) solution for 60 seconds at 23°C, whose the schematic is shown in Figure 3-11(a). Subsequently, the pattern is transferred by two-step etching. The HSQ layer is etched by RIE in CF_4 plasma shown in Figure 3-11(b), and then pattern transferred to a-Si by inductively coupled plasma (ICP) RIE with gas mixture of $SiCl_4$ and Ar for better etching selectivity and vertical sidewall as shown in Figure 3-11(c). The $SiCl_4$ gas can form Cl inhibitors on the structure sidewall against lateral etching, and the bombardment of Ar helps on creating a vertical sidewall [38, 39]. In addition, the SiO_2 underneath the a-Si acts like an etching stop due to the high selectivity between a-Si and SiO_2 in $SiCl_4$ plasma. Micro-loading effect can be eliminated by over-etching for 30 seconds. Last as shown in Figure 3-11(d), a 10nm-thick Si_3N_4 layer is deposited by PECVD to reduce the waveguide sidewall roughness scattering [37]. The recipe about the process will be presented in Appendix B.

3.3.2 Point Spread Function Measurement and Proximity Effect Correction for Rod-slab Lüneburg Pattern

In principle, the negative-tone resist such as HSQ was cured by the energy of secondary electrons scattered by the material stack from the incident electron beam. The total dose distribution of any exposure is the convolution of exposure dots of

the pattern and the spatial distribution of energy dissipation by the beam, *i.e.* Point Spread Function (PSF), which can be represented as

$$D(x, y) = \text{PSF(x,y,)} \circledast \text{Ptn}(x, y) \tag{3.2}$$

where $D(x, y)$ is the dose distribution over the exposed sample, $\text{PSF}(x, y)$ denotes the point spread function of the beam, and the $\text{Ptn}(x, y)$ means exposure dots of the pattern. If the pattern on the layout is too dense, the contribution of the dose from desirable places is going to provide the additional dose for the undesirable area as shown in Figure 3-12(a). As long as the dose accumulation is over the resist

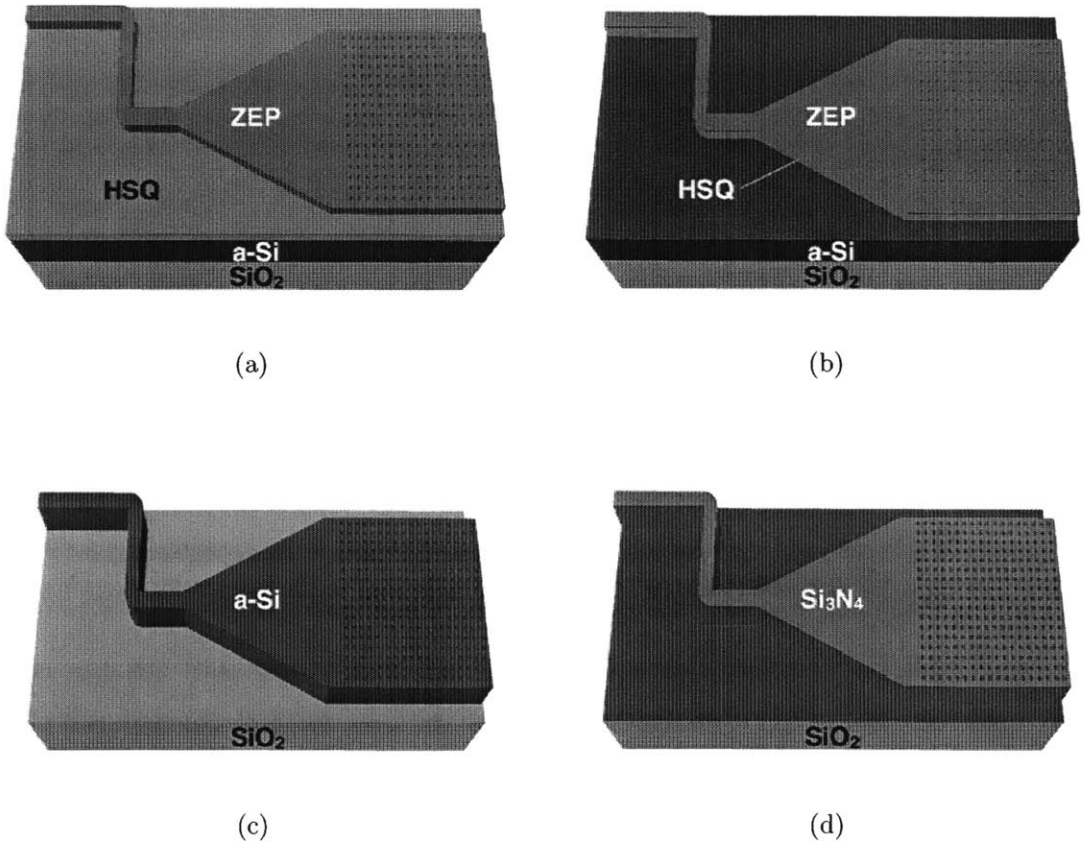

Figure 3-11: Process flow for hole-slab Lens (a) Pattern the device by e-beam lithography on ZEP resist (b) Etching HSQ layer by RIE with CF_4 plasma (c) Etching the a-Si layer by ICP-RIE with $SiCl_4$ and Ar plasma (d) Deposition of Si_3N_4 by PECVD for decreasing surface roughness scattering.

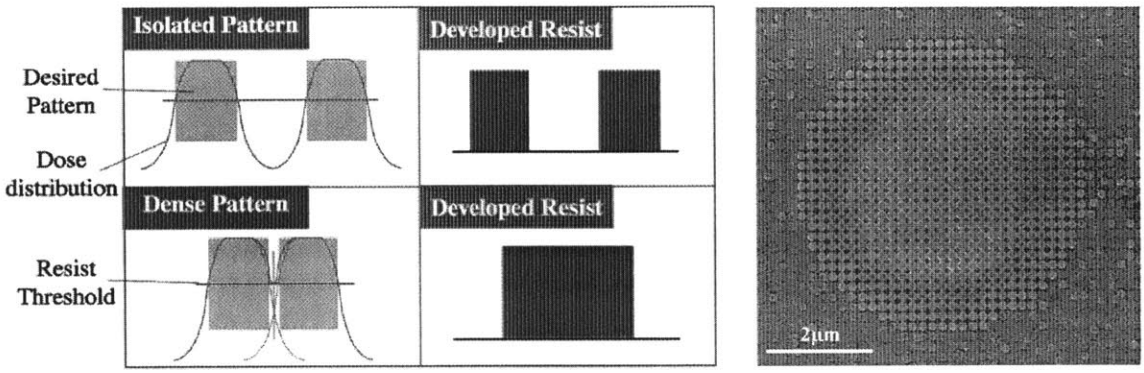

Figure 3-12: Proximity effect of e-beam lithography (a) Schematics for dose distribution of isolated and dense patterns (b) Preliminary exposure results for rod-slab lens.

threshold, two originally distinct patterns can not be resolved after development. This phenomenon is known as proximity effect (PE).

The first exposure result of the rod-slab Lüneburg lens as shown in Figure 3-12(b) is not going well as expected even with the dose matrix test. Obviously, ambient HSQ rods around the lens region were underdosed, but center HSQ rods were overdosed, and this is the evidence of the PE due to the uneven distribution of exposure dots from e-beam lithography. In order to control the PE, we need to characterize the PSF in this case, which is determined by the material stack and the characteristic of the e-beam writer. We fixed all parameters such as the thickness of HSQ, a-Si, and SiO_2 with constant projection voltage of 125 kV and current at 400 pA from our e-beam writer (Elionix ELS-125F) to measure the PSF. The measurement is performed using dot exposure with increasing dose time in terms of the power of 1.2 times with the distance of 300 μm apart to avoid dose interference from other exposure, and the range of the dose time varies from 0.1 μs to 948 seconds interpolated by 124 points. The measured PSF as shown in Figure 3-13 is fitted and overlaid by the Eq. (3.3) consisting of the sum of two Gaussians, and an exponential term, and a term equivalent in appearance to the frequency of a 2-pole low-pass filter

$$A\left(\frac{1}{\sigma_1^2}e^{-\left(\frac{r}{\sigma_1}\right)^2}+\frac{\eta}{\sigma_2^2}e^{-\left(\frac{r}{\sigma_2}\right)^2}\right)+Be^{-\frac{r}{r_e}}+\frac{C}{\sqrt{1+(r/r_f)^4}} \tag{3.3}$$

was found to fit our measured data [40], where $A \cong 1.1 \times 10^{-2}$, $\sigma_1 = 1.24$ nm, $\eta = 5.29 \times 10^{-3}$, $\sigma_2 = 46.51$ μm, $B = 3.49 \times 10^{-2}$, $r_e = 5.47$ nm, $C = 3.49 \times 10^{-1}$, $r_f = 1.12$ nm. σ_1 indicates the beam spot size and the lateral extent of forward scattering, and σ_2 indicates the lateral extent of backscattering [41]. The exponential term may indicate Beer-Lambert-like absorption of secondary electrons with r_e as the mean free path. The filter term is phenomenological; its physical meaning is unclear, but it is important in accurately fitting the PSF between $r = 50$ nm and $r = 10$ μm.

After characterizing the PSF of the e-beam machine, the dose distribution of the rod-slab Lüneburg pattern as shown in Figure 3-14(a) could be simulated from convolving the layout with the measured PSF. The dose received around the lens center is almost twice higher than that in the ambient area. The proximity effect correction (PEC) can be performed by deconvolution of Eq. (3.2), which is rewritten as,

$$D_{re}(x,y) = \mathscr{F}^{-1}\left\{\frac{\mathscr{F}\{D_{tg}(x,y)\}}{\mathscr{F}\{\mathrm{PSF}(x,y)\}}\right\} \tag{3.4}$$

where $D_{re}(x,y)$ is the real dose distribution over the exposed sample after PEC, the

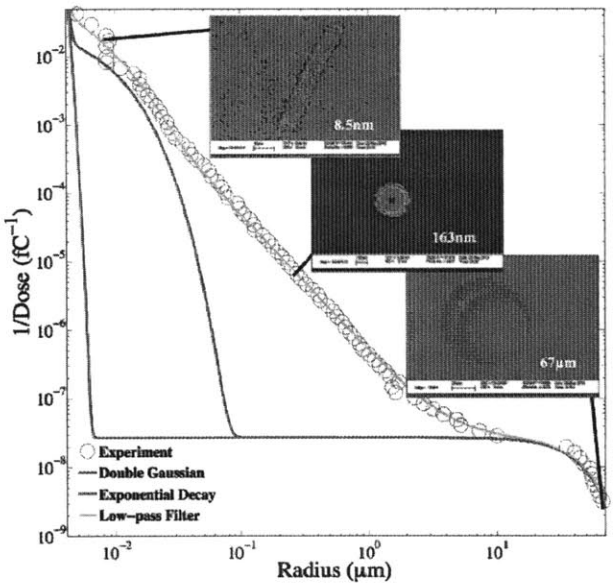

Figure 3-13: The measured PSF is denoted by the dose reciprocal function of the radius of exposed rods, which is measured under the secondary electron microscopy.

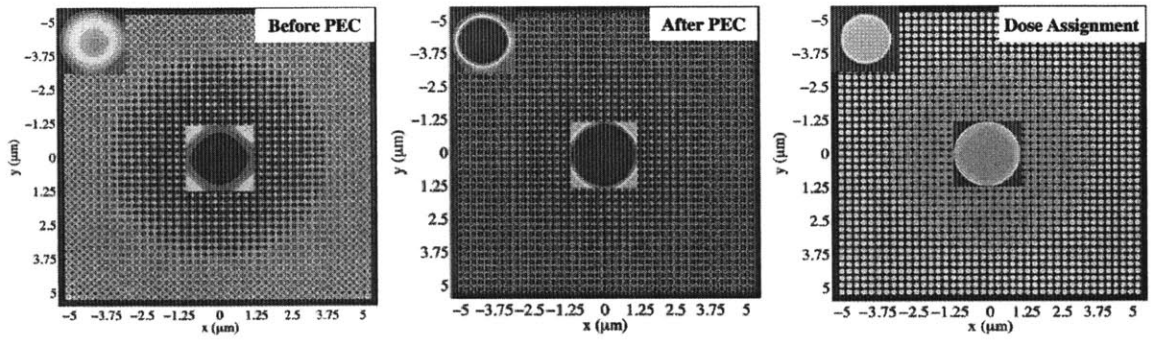

(a) (b) (c)

Figure 3-14: Dose simulation for the rod-slab Lüneburg lens using measured PSF to convolve with the pattern layout (a) without correction (b) with correction (c) Assigned dose map after correction. Enlarged pictures represents the rod at corner and center, respectively.

$D_{id}(x, y)$ means the ideal dose distribution for the pattern, and PSF(x, y) still denotes point spread function of the beam. Here, the ideal dose assignment is assumed as the 0 and 1 for without and with pattern on the layout, respectively. Simulated results and corresponding dose map after PEC are shown in Figure 3-14(b) and (c). Moreover, the real exposure and the following etching are also performed on HSQ and a-Si as shown in Figure 3-15. Results show that central rods cannot be resolved completely even with PEC, and this could bring measurement errors during characterization.

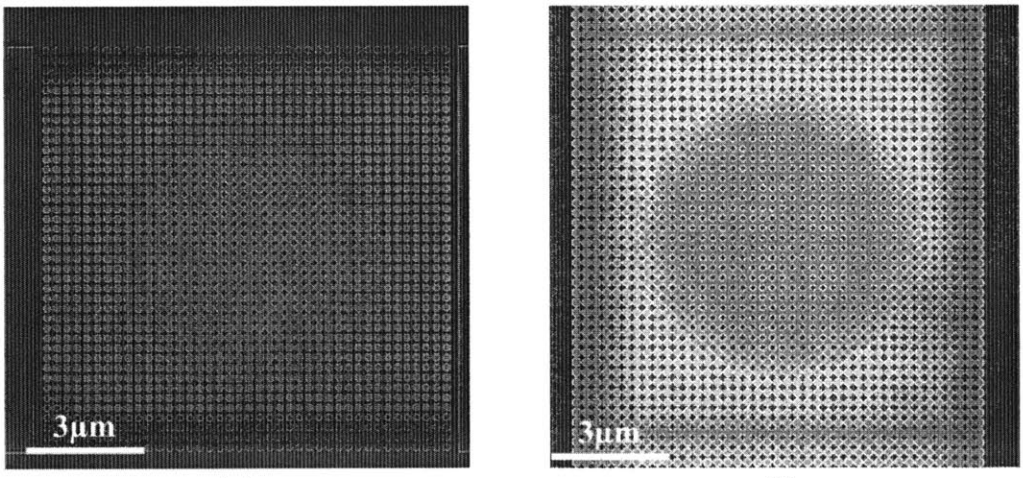

(a) (b)

Figure 3-15: Proximity effect correction for rod-slab Lüneburg pattern (a) on HSQ (b) Transferred to a-Si.

The root cause of the problem results from the blur of the HSQ and dense pattern that is hard to resolve.

3.3.3 Fabrication of hole-slab Lüneburg lens

Because of the fabrication challenge on rod-slab pattern, the hole-slab Lüneburg pattern is an alternative for a better prototyping of nanostructured Lüneburg lens. The positive resist ZEP-520A was used for the hole-slab fabrication because now the exposed area should dissolve instead of remaining during development. A positive-tone resist like ZEP-520A could have much lower dose to clear the exposed resist. As described in the previous section, a durable hard mask for structure etching was used. FOX-14 from Dow corning is a kind of liquid oxide but not for exposure purpose due to the low contrast. Lithograph and etching results were shown in Figure 3-16 and 3-17, respectively.

While etching the device layer, using the $SiCl_4$ gas only resulted in the wedge shape of the coupling waveguide. The dimension increase at the bottom of the coupling waveguide could have another mode existing to detain the integrity of the il-

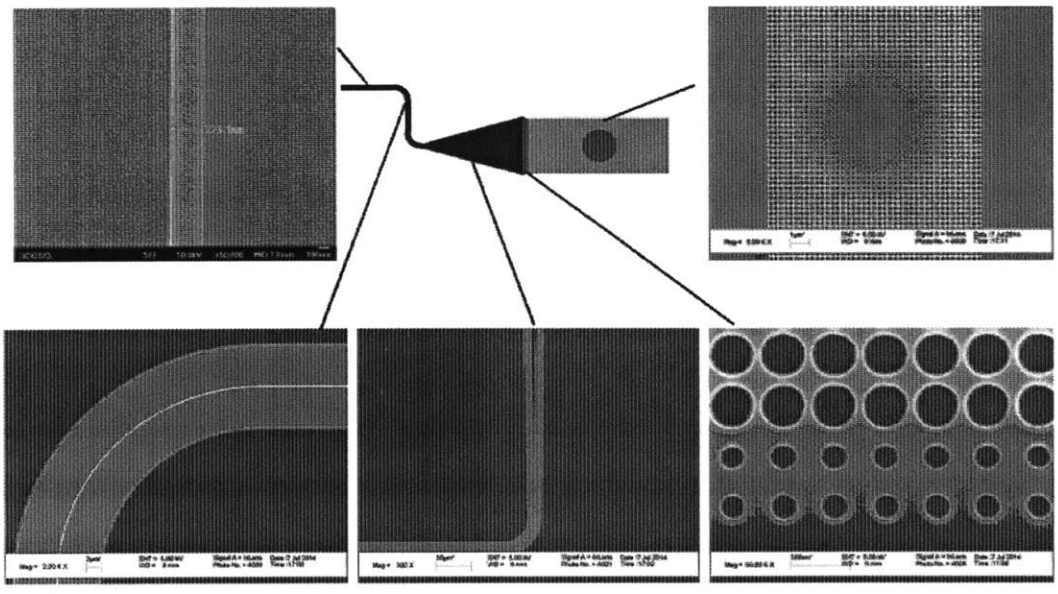

Figure 3-16: Lithography results of hole-slab Lüeburg pattern. The coupling, bend, and tapered waveguide are all shown here. Holes around lens center are also clearly resolved without doing the PEC.

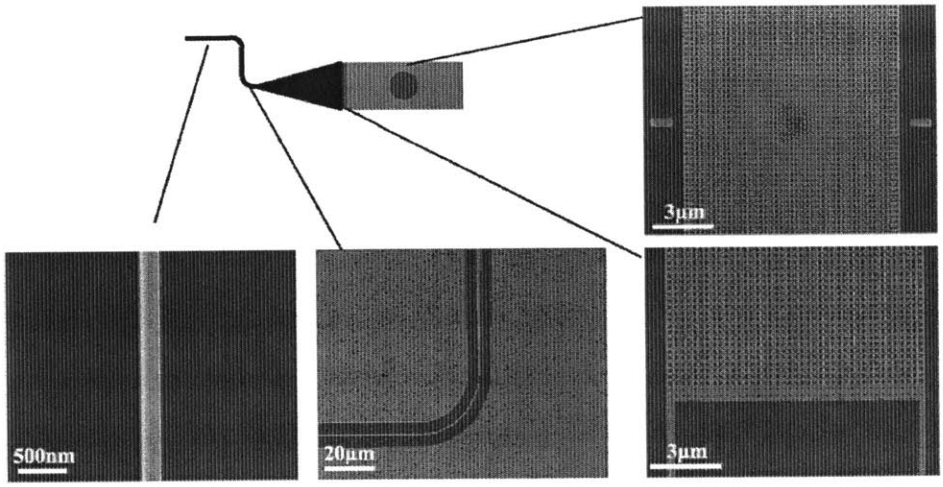

Figure 3-17: Etching results of hole-slab Lüeburg pattern. All components in the design were successfully transferred to the device layer.

lumination. After introducing the Ar gas to destroy the protection layer form by Cl atoms, the vertical sidewall was obtained. The modal analysis for both cross-section were performed by MPB mode solver as shown in Figure 3-18. The wedge

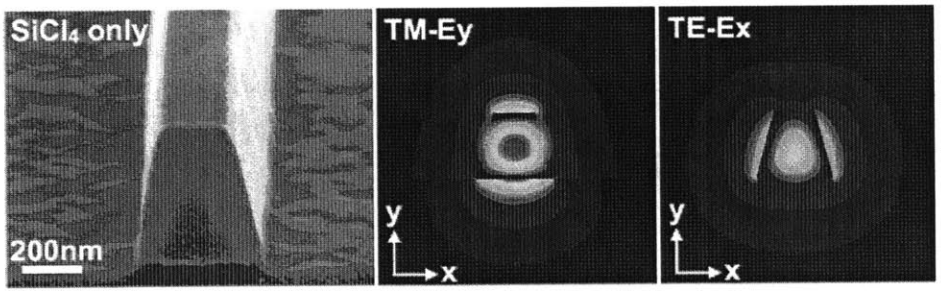

(a)

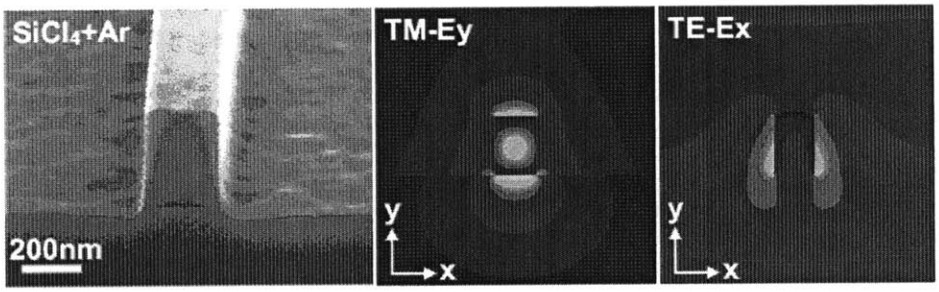

(b)

Figure 3-18: Modal analysis of wedge and rectangular waveguide. Cross-section and their modes simulated by MPB were shown here for (a) Wedge (b) Rectangular waveguide, respectively.

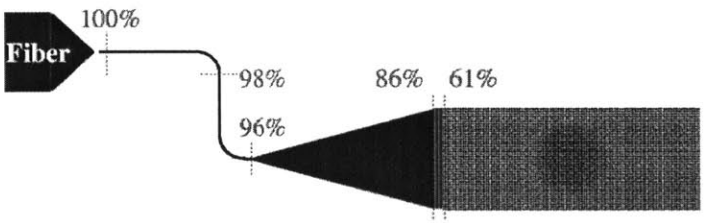

Figure 3-19: The transmission check at the end of each device was performed by Lumerical FDTD software.

cross-section was found that it can contain two fundamental modes from TE and TM separately. The rectangular waveguide only allows the TM fundamental mode to propagate, which is consistent with the purpose of our design. In addition, we also simulated the transmission of each component using Lumerical FDTD software to ensure the fraction of power that arrives at the entrance of the lens region as shown in Figure 3-19. Most of the lost results from the EIR difference between the tapered and hole-slab waveguide, which is 3.07 and 1.7 in this case. Thus, we designed an antireflective layer in between to eliminate the reflection so that there is still 60% of light that can transmit to the lens region.

3.4 Characterization

The characterization of the nanostructured Lneburg lens is carried out by near-field scanning optical microscopy (NSOM) so as to investigate the wave behavior of our design as shown in Figure 3-20. The as-fabricated sample is cleaved along the transverse plane of the coupling waveguide to ensure a clean facet for light coupling. A lensed fiber butt-coupled with a 1550 nm laser diode (FPL-1009S, Thorlab Inc.) is positioned in a working distance of 14 μm with respect to the waveguide facet using the stage driven by piezoelectric motor. The evanescent field and scattered light over the lens region are collected by a bent fiber tip with 300 nm in diameter and Cr coating over the tip sidewall. This fiber tip assembly is mounted on the NSOM system (Multiview 4000, Nanonics Imaging Ltd.), and the NSOM tip is operated in tapping mode at a distance of 20 nm from the structure top surface. The optical signal is

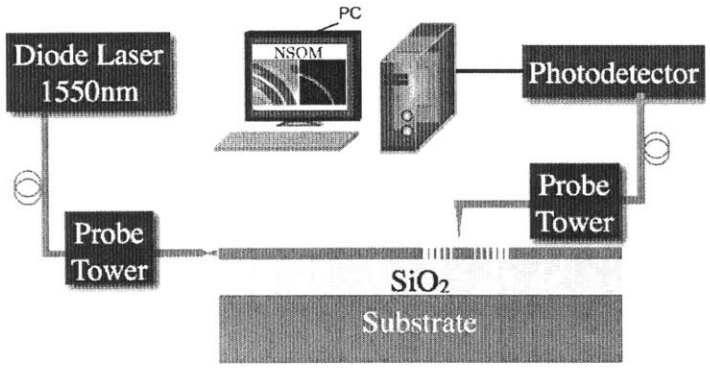

Figure 3-20: Schematics of near-field scanning optical microscopy.

detected by an amplified InGaAs photodetector (PDF10C, Thorlab Inc.). Figure 3-21(a) shows the combined collected light and topographical information collected by this NSOM from our sample.

If the tip diameter is larger than the wavelength image blur results. If the tip

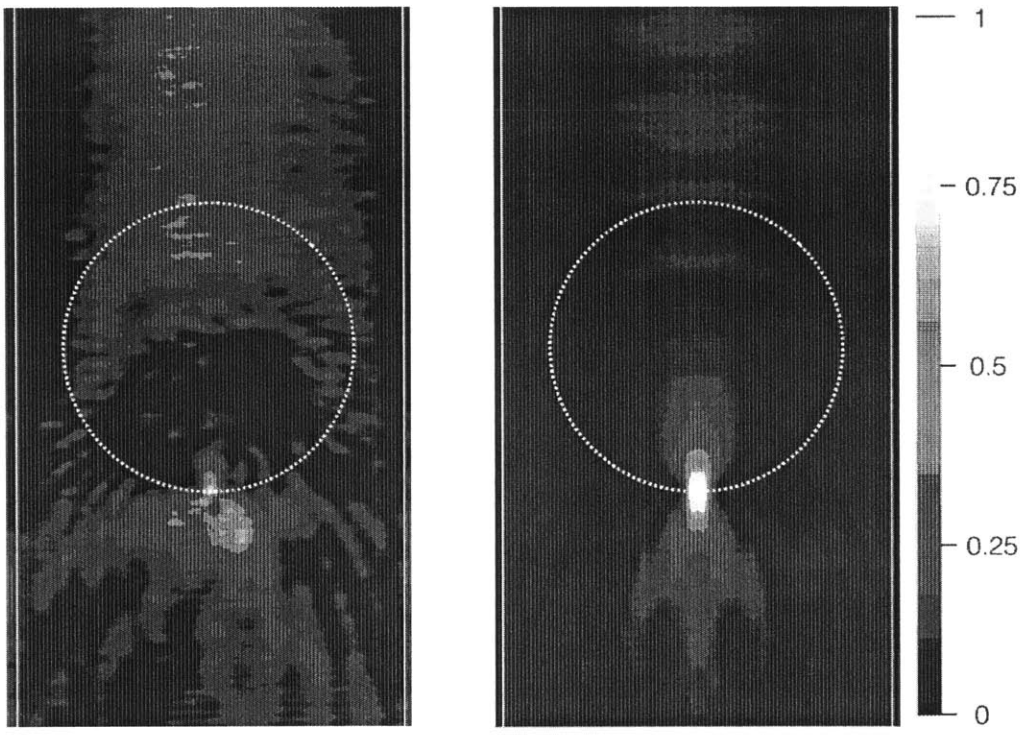

(a) (b)

Figure 3-21: Modal analysis of wedge and rectangular waveguide. Cross-section and their modes simulated by MPB were shown here for (a) Wedge (b) Rectangular waveguide, respectively.

diameter is smaller than the wavelength coupling is weaker and the image becomes noisier. We chose the scanning step size to be 60 nm (*i.e.* 1/5 of the tip diameter) as a good compromise against the low signal problem. Comparing Figure 3-21 (a) and (b), the differences are striking. First, two period of the interference pattern that is evident in the NSOM measurement approximately half the period of the wave in the simulation. This is because in the experiment inevitable reflections from the interferences cause standing wave patterns, whereas in the simulation reflections were eliminated by use of a perfectly matching layer (PML). The second striking difference is the much darker pattern inside the lens region observed in the simulation as compared to the experiment. This is because the calculation of Figure 3-21 (b) is the intensity at a single plane located at the nominal tip-surface distance of 20 nm; whereas the actual measurement vertically integrates light scattered throughout the

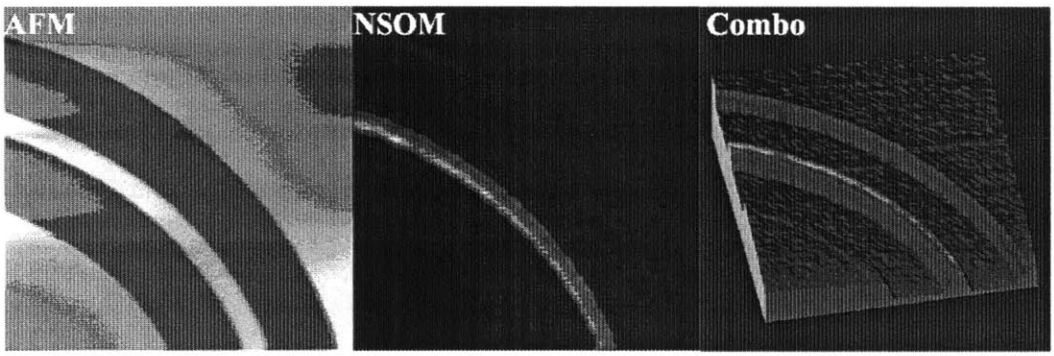

(a)

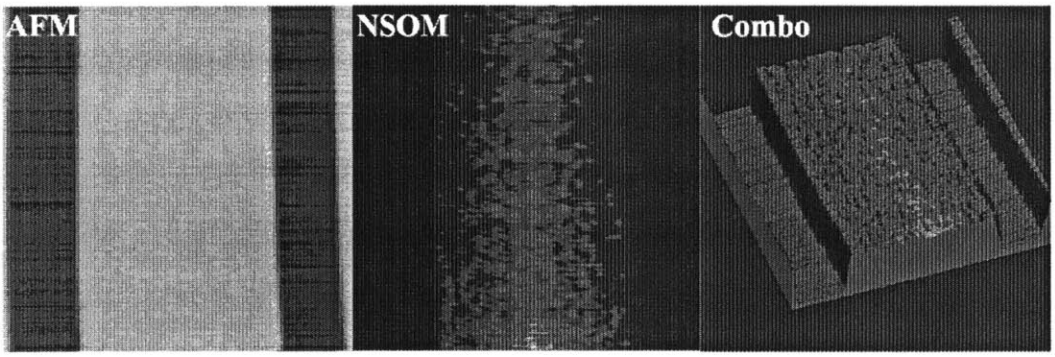

(b)

Figure 3-22: NSOM results includes the topologcal (AFM) and optical (near-field) information, and their combination for a 3D profiling (a) Bend waveguide (b) Part of tapered waveguide.

structures entire volume. Since the EIR at the lens center is higher, the vertically integrated intensity in that region is also higher, explaining this regions brighter appearance in the NSOM measurement.

We not only measure the images around the lens area, but also collect the data from the other components in our design. The image for bend waveguide as shown in the Figure 3-22 indicates that light propagation is perfectly isolated from waveguide to adjacent a-Si by the air trench. The

3.5 Hamiltonian Ray-Tracing Results

3.5.1 High-order mode illumination

The near-field behavior of the nanostructured Lüneburg lens has been measured successfully, but there are some phenomena in the NSOM image that had not been expected. Although we retain the integrity of the illumination carefully with a ta-

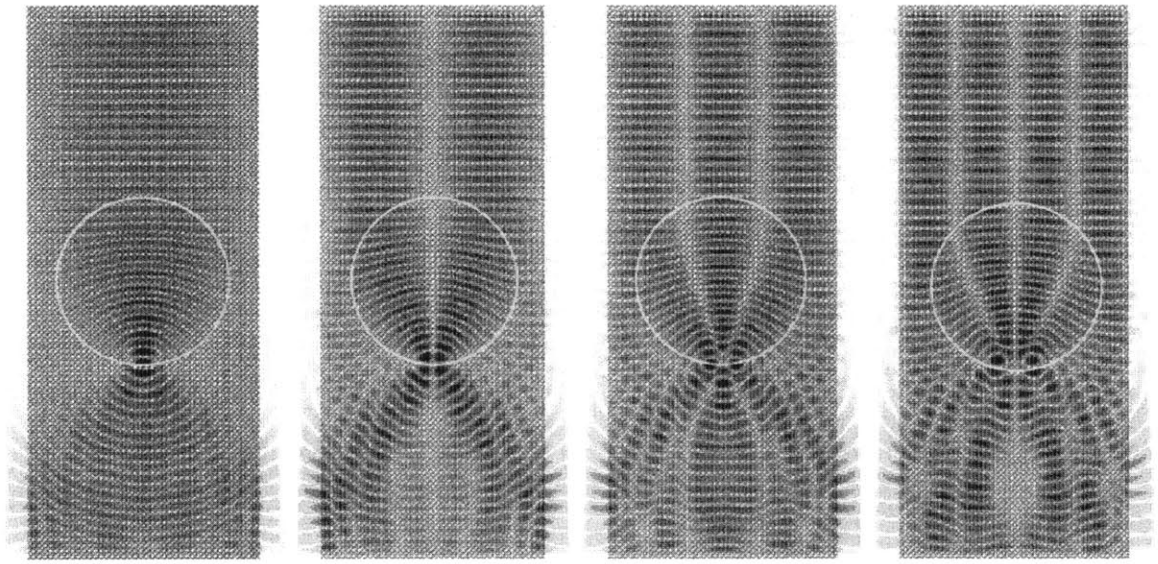

(a) (b) (c) (d)

Figure 3-23: The modal analysis of rod-slab Lüneburg lens under different order of illumination denoted by field plot (a) Fundamental (b) First (c) Second (d)Third mode. Fields from 2D simulation can approximate to the field at the center of the 3D slab.

pered feed, the close EIR between each modes in the multimode waveguide could result in the crosstalk due to scattering or imperfection of the fabricated structure. In order to understand light propagation under multimode illumination along the rod-slab waveguide shown in Figure 3-21(a), we analyze different modes that satisfy the guiding condition of the rod-slab waveguide and their corresponding field distributions using FDTD method. The MPB and MEEP were used again in this analysis. Basically, the mode computed from MPB was fitted by a polynomial function that was carried out by MATLAB, and this polynomial function was fed into MEEP as a new source instead of using a plane wave to emit the light from the original source plane. There was a space spared for light propagation along the rod-slab waveguide to eliminate instability or discontinuity at the side of the waveguide generated from the embedded light source.

In order to save computation time without losing the physics, a 2D rod-slab Lüneburg lens was used for simulation. Results as shown in Figure 3-23 and 3-24 represented fields and intensities of modes in nanostructured Lüneburg lens illumi-

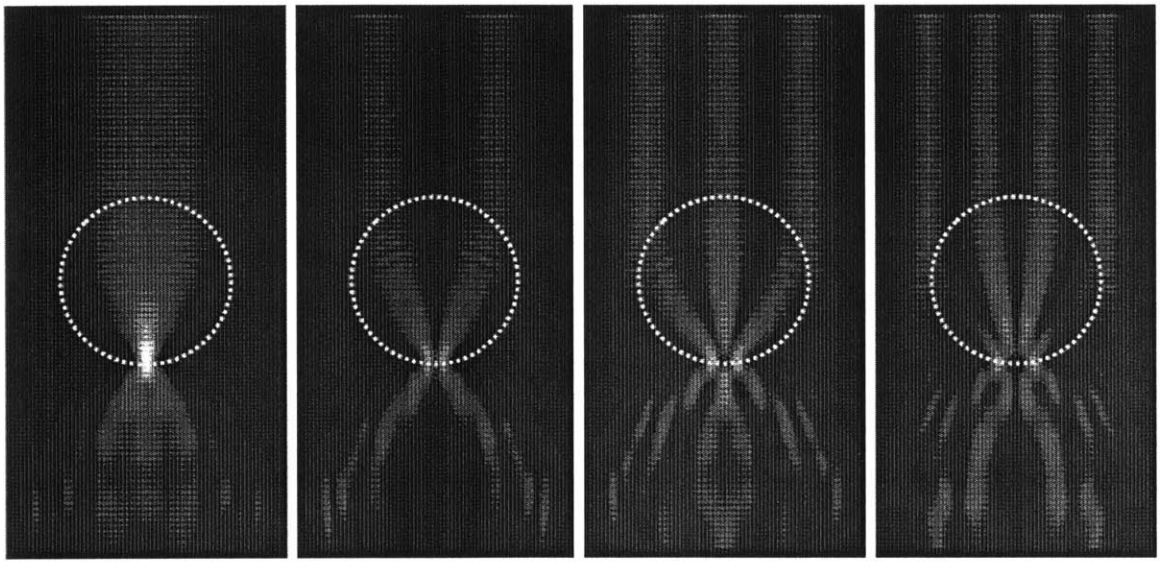

(a) (b) (c) (d)

Figure 3-24: The modal analysis of rod-slab Lüneburg lens under different order of illumination denoted by intensity plot (a) Fundamental (b) First (c) Second (d)Third mode. Intensities from 2D simulation can approximate to the intensity at the center of the 3D slab.

nated by different order of light modes. It was observed that the two foci phenomenon happened while high-order mode of light illuminated the lens. In comparison of simulated Figure 3-24(d) and NSOM image 3-21(a), the interference pattern around the lens side was highly matched with the third-order mode illumination. The modal illumination is hard to get rid of completely, but the integrity of the illumination could be kept at high purity if:

(1) The dimension of the coupling waveguide is well-controlled as discussed in the fabrication section.

(2) The propagation distance of the slab waveguide is not long enough to provide higher chance for crosstalk. In the design, we only spared 15 μm (10 wavelengths) for the stable and pure illumination.

3.5.2 Wigner distribution function

The Fourier transform is generally used for the analysis of frequency response, and it will give us the information about the component of frequencies over the spectrum in the whole system. However, it sometimes only needs local frequencies to evaluate the optical behavior of the system. The Wigner Distribution Function (WDF) is not only used in quantum mechanics in phase space, but also can deal with the position-momentum and time-frequency pairs in optics. The WDF is defined as [42, 43, 44]:

$$\mathcal{W}(x,u) = \int \psi\left(x+\frac{x'}{2}\right)\psi^*\left(x+\frac{x'}{2}\right)e^{-i2\pi x'u}\,dx' \tag{3.5}$$

where ψ is the complex field from the source plane, the x denotes the transverse position of the mode, u indicates the spatial frequency at corresponding position x, and the $\mathcal{W}$ represents the WDF as a general irradiance.

Herein, the WDF was used in this section to translate the complex field in space to essential local spatial frequencies along with their position for the ray-tracing. Take the rod-slab Lüneburg lens for instance. Substituting the complex field acquired from the source plane in Figure 3-23 into Eqn. (3.5), the WDF from each mode as shown in

Figure 3-25 can provide the initial condition, which the general irradiance is function of the momentum and position for ray-tracings. It is also very interesting to directly analyze the complex field in each transverse plane of FDTD simulations to see the change of the WDF as shown in Figure 3-26. The WDF of the fundamental mode starts rotation during focusing within the lens region, and then all waves come to the focal point, *i.e.* the edge of the lens region, with the different spatial frequencies. After passing the focal point, the shearing WDF represents the divergence after focus, which is also the common property in WDF plot.

3.5.3 Hamiltonian ray-tracing results

Hamiltonian ray-tracing with the Wigner distribution function (WDF) is the next step to translate the wave behavior into a ray diagram, which is physically more intuitive [45, 46, 47]. The WDF defines the generalized irradiance that is the function of positions and momenta. Ray tracing can be performed using Hamiltonian equations:

$$\frac{d\mathbf{q}}{dz} = \frac{\partial H}{\partial \mathbf{p}}, \quad \frac{d\mathbf{p}}{dz} = -\frac{\partial H}{\partial \mathbf{q}} \tag{3.6}$$

where z means the propagation direction, $\mathbf{q}$ denotes the ray position, $\mathbf{p}$ is the ray momentum, and the H is the Hamiltonian consisting of kinetic and potential energy in the wholes system. If we still use the 2D assumption along with the WDF computation

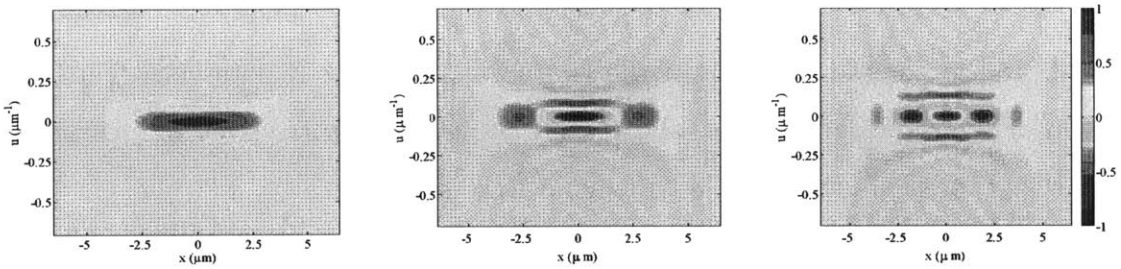

(a) (b) (c)

Figure 3-25: The Wigner distribution function computed for TM-like polarization in rod-slab Lüneburg lens (a) Fundamental mode (b) The first mode (c) The second mode. Colorbar denoted at the side shared by three plots.

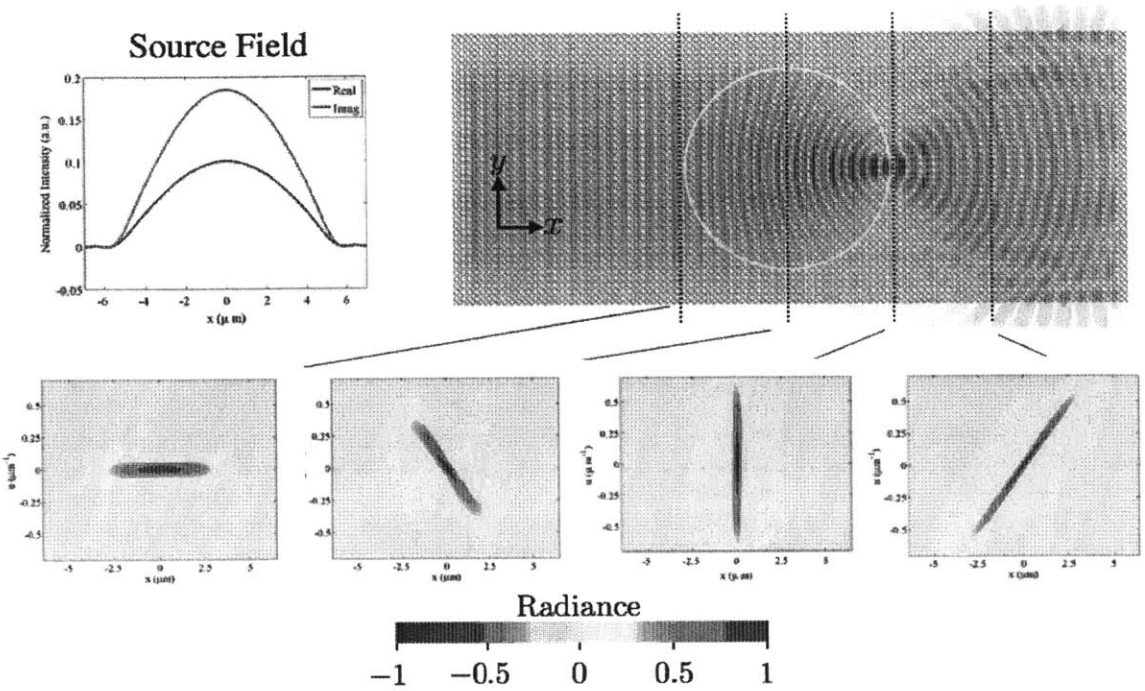

Figure 3-26: WDF change along with the nanostructured Lüneburg lens. The WDF undergoes the rotation (within lens) and shearing (after focusing) during the propagation.

in the previous section, we can directly convert 3D Hamiltonian to *screen* Hamiltonian as [48]

$$H = -\sqrt{n^2(\mathbf{q}, z) - |\mathbf{p}|^2} \tag{3.7}$$

For the Lüneburg lens, $n \equiv n_0\sqrt{2 - (r/R)^2}$ as shown in Eqn. (1.2). With initial positions and momenta of rays defined by the WDF at the source plane shown in Figure 3-25. Results are shown in Figure 3-27 for the fundamental and second order mode, respectively. For the fundamental mode illumination, ray-tracing results as shown in Figure 3-27(a) also reveal a single focus as well as the FDTD simulation as shown in Figure 3-24. For the second-order mode illumination, it can be observed intuitively in Figure 3-27(b) that the focusing of rays carrying positive radiances result in bi-foci, and the irradiance at the right edge of the lens has been partially cancelled out by rays carrying positive and negative radiances, resulting in the intensity dip in Figure 3-24(c). The same method can also be applied for analyzing other modes and a combination of them existing in our system.

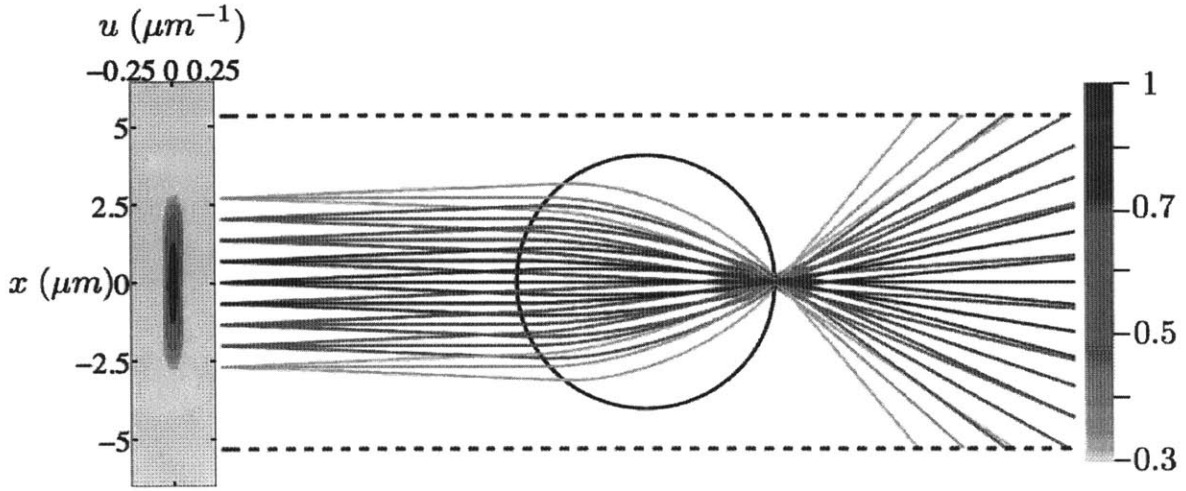

(a)

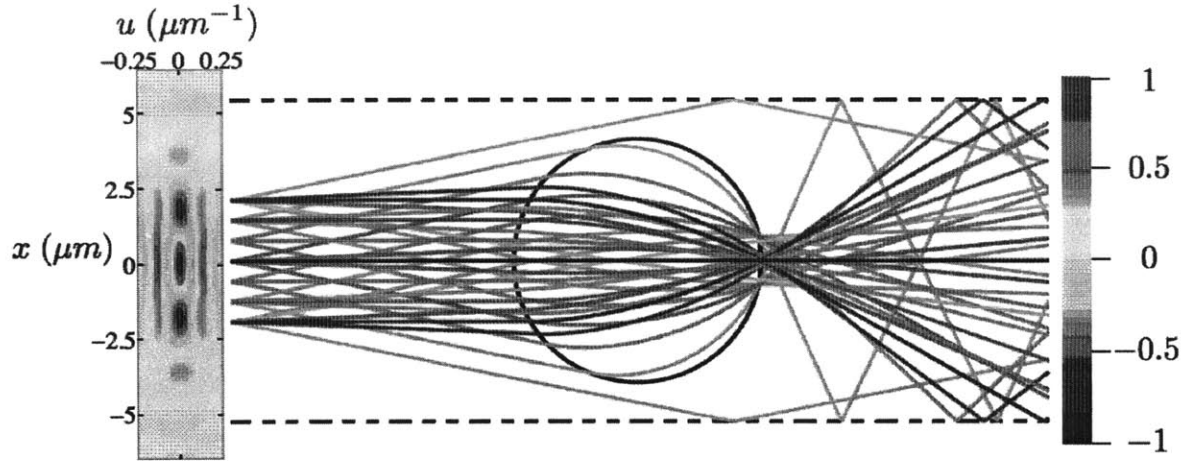

(b)

Figure 3-27: Hamiltonian ray-tracing results with (a) Fundamental (b) Second-order mode illumination. Rays with positive and negative radiances generated from WDF at the source plane (left-hand side) propagate toward the lens to show the cancellation at focal point, which explains the bi-foci behavior in the high-order mode. Color bar at the right denotes the normalized general radiances.

3.6 Summary

In conclusion, a nanostructured Lüneburg lens was designed as an a-Si nanorod and nanohole array with varying structure diameters to achieve the effective index of refraction at each coordinate location, based on an direct bandgap diagram method

to compensate for the thin-film effect. The complete design included a coupling waveguide for excitation integrity and a 300μm-long tapered waveguide for single mode evolution. Between two waveguides, there is a 200 μm offset by bent waveguides to decrease the crosstalk from the fiber source. The entire structure was patterned using e-beam lithography followed by a two-step etching processes, including RIE and ICP-RIE to ensure that the waveguide walls are vertical. The as-fabricated device was characterized by NSOM to map the evanescent and scattering light over lens region with topography. Experimental results showed good agreement with FDTD simulation. The post-analysis using Wigner distribution function and Hamiltonian ray-tracings explained the bi-foci behavior of the Lüneburg lens under the high-order mode illumination.

THIS PAGE INTENTIONALLY LEFT BLANK

Chapter 4

Conclusions and future work

Film and slab GRIN materials were investigated in this dissertation for two different applications: light extraction and planar focusing component. Both topics not only involved with a very extensive understanding on multiple disciplines, but also required plenty of practical experience for proof of concept. Continuing the prior work from former researches, the author did not walk through the ideal model by simply revising their assumption. Instead, the author integrated the design, simulation, fabrication, and characterization in order for implementation. The old problems with a modified but not consolidated tool existed in the aspect of design and characterization for better improvement, and other unforeseen challenges on fabrication and simulation were waiting for exploration. Major contributions of this work included:

- Hybrid structure for enhancing extraction efficiency of the scintillator
  - Integrated the antireflective and diffractive characteristics from different structures together to retend the great performance from the photonic slab to a better outcome using proposed hybrid structure.
  - Combined nanosphere and laser interference lithography for complex patterning, which is expected hardly to succeed at the beginning.
  - Fulfilled the requirement for large area patterning, parallel exposure with relatively shorter time and batch fabrication.

- Much more durable structure using inorganic material compared to the work done by nanoimprint and feasible with state-of-the-art manufacturing in industry.

- Nanostructured Lüneburg lens

  - Applying the Wigner distribution function and Hamiltonian equations to a practical design for ray behavior translation. The problem from modal illumination, *i.e.* the bi-foci phenomenon, has been studied by FDTD simulation.

  - Proposed to use the fundamental illumination in both simulation and emulation, to prevent the bi-foci phenomenon from the characterization. In the mean time, scaling the simulation scope up to meet the practice.

  - Challenged the impractical rod-slab design with proximity effect correction, and then implemented the alternative hole-slab design to yield an expected single focus in the measurement.

  - Consider the entire device for characterization carried out by NSOM. The mode was carefully controlled and retained by coupling and tapered waveguide to result in a satisfying focus image with NSOM vibration noise.

Beyond the accomplished scope, the experience and techniques resulting from this work can also apply to other engineering problems that consist of the similar challenges. Some future work may include

- Film GRIN

  In addition to the scintillator, the same problem also occurs in light extraction from LED source. In order to satisfy the sustainable development and environment friendly requirement, energy-saving is always the top issue that engineers pay attention to. LED has been generally used as light source everywhere to replace with traditional halide and cold-cathode fluorescent lamps. Enhanced light extraction can be integrated from the component to system level. With

the experience on antireflection and light extraction, the specific problem that requires these two benefits will have a novel solution.

- Slab GRIN

  We studied both hole and rod design separately, but have not explored the complimentary design for their practical applications. In addition, guiding the wave using Lüneburg lens is a popular function in microwave frequencies. However, source tracking at mid-infrared range using Lüneburg lens is under exploration. We can expect to use a new material such as germanium for the light manipulation.

THIS PAGE INTENTIONALLY LEFT BLANK

Appendix A

List of Abbreviations

APT	Avalanche PhotoDetector
a-Si	Amorphous Silicon
c-Si	Crystalline Silicon
EIR	Effective Index of Refraction
FDTD	Finite Difference Time Domain
GRIN	GRadient INdex
HSQ	Hydrogen SilsesQuioxane
ICP	Inductively Coupled Plasma
LED	Light Emitting Device
MEEP	MIT Electromagnetic Equation Propagation
MPB	MIT Photonic-Band
NSOM	Near-field Scanning Optical Microscopy
PEC	Proximity Effect Correction
PMT	PhotoMultiplier Tube
PML	Perfect Matching Layer

PSF	Point Spread Function
RIE	Reactive Ion Etching
SEM	Secondary Electron Microscopy
SOI	Silicon-On-Insulator
TE	Transverse Electric
TIR	Total Internal Reflection
TM	Transverse Magnetic
WDF	Wigner Distribution Function

Appendix B

Fabrication Summary

Contents

All processes developed in this dissertation are mostly done using MIT facilities that distribute in Technology Research Lab (TRL), Exploratory Material Lab (EML), and NanoStructure Lab (NSL). Some abbreviations used in the process are Antireflective Coating (ARC), Photo Resist (PR), Reactve Ion Etching (RIE), Inductively Coupled Plasma (ICP), and Scanning-Electron-Beam Lithography (SEBL).

B.1 Surfactant Treatment of Nanospheres

The surfactant treatment for nanospheres plays an important role to the deposition quality. The recipe listed here is only available for the silica beads. Bead made by

other material like polymer or metal should not share the same process unless they have the same amphiphilic property after the same treatment. The protocol was referred to the Johnathan Mailoa's master thesis in MIT with special acknowledgement to his fruitful discussion [49]. The entire treatment process are outlined here:

1. Disperse 160 mg silica beads with 100 nm diameter (Fiber Optic Center Inc.) in 10 ml of ethanol in a 20 ml glass vial.
2. Add 0.4 ml APTES ((3-Aminopropyl)triethoxysilanethe, 98%, Sigma-Aldrich) and 4ml deionized water into the colloidal solution.
3. Ultrasonicate the colloidal solution for 5 min to segregate beads.
4. Stir the colloidal solution with magnetic stick for 8-12 hours to completely mix the APTES with solvent.
5. Heat up the colloidal solution up to 100°C with the cap for 3 hours to functionalize APTES on silica beads.
6. Centrifuge the solution and replace the solvent with methanol for 3 times.
7. Segregate the final solution via ultrasonication before the injection.

Notes:

- The temperature of the heating process is key to functionalization.
- The evaporation is under control with the cap even the vaporization point of the ethanol is 75°C.
- It's better to use the fresh as-treated beads for coating process because the quality of functionalization might degrade after few days.

B.2 Langmuir-Blodgett Deposition

The Langmuire-Blodgett deposition in this work was carried out by the KSV NIMA 312 from Biolin Inc. including a trough and controller. In order to gently disperse

the beads over the water surface, a injection pump for controlling the flow rate was also used here. Here is the procedure for deposition:

1. Clean the trough using the methanol with sterile wipe to eliminate the pollution from debris or fibers.
2. Fill the trough with deionized water untill the Wilhelmy plate touches the water surface.
3. Boot up the software to connect the trough controller with right communication port.
4. Check the pressure sensor reading around -72 mN/m at the beginning followed by zeroing the reading.
5. Move the compression bar to "close" and "open" position to ensure the pressure variation less than 0.5 mN/m. If not, use the suck tube to draw some water out from the surface at "close" position for extracting suspended particles out.
6. Move the compression bar to "open" position if the pressure variation between the open and close position is less than 0.5 mN/m.
7. Fill the syringe with the as-treated colloidal solution and mount the teflon tubing on the syringe needle.
8. Pump out the solution at flow rate of 80 ml/min after fixing the syringe on the pump and taping tubing exit close to the water surface, while the compression is still at the open position.
9. Stop feeding the solution until the pressure reading up to 2-3 mN/m.
10. Activate the sample surface hydrophilically by a 3 min O_2 plasma treating.
11. Start the sample dipping before assembling the bead.
12. Initialize the pressure control function targeting at 15 mN/m for silica beads by software.

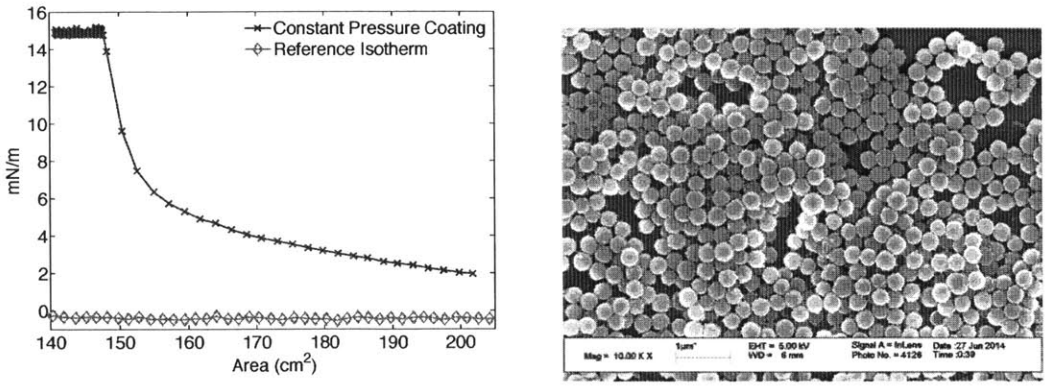

(a) (b)

Figure B-1: Langmuir-Blodgett deposition (a) Isotherm plot for clean reference and a successful coating under pressure control (b) Multilayer results assembled on an Al-coated glass slide when the surface pressure at 20 mN/m.

13. Raise the sample up creepily at the speed less than 5 mm/min for the first sample coating.

14. Move the bar out and repeat the step 8 to 13 if the second coating is under way.

15. Suck the suspended particles out at close position with the attention to the water surface not lower than the bar in case of particle leakage out to outer position.

16. Remove the whole water out after the pressure reading less than 0.5 mN/m.

17. Wipe the trough before covering. Power down the all the instruments.

The initial cleanness is important for predicting the beads density after injection. The isotherm that depicts the surface pressure function of compression position as shown in Figure B-1(a) is usually used in the Langmuir-Blodgett deposition to describe the assembly condition. The red diamond line indicates a clean trough ready for deposition, which the surface pressure keeps constant within a variation of 0.5 mN/m. Another blue cross line indicates the isotherm under the pressure control using the compression bar. While the surface pressure begins to increase exponentially, the monolayer forms on the water surface. If the bar keeps compressing, it will exceed the highest pressure affordable for the monolayer condition depending on the bead

material. In this work, 15 mN/m works pretty well for a monolayer coating of silica beads. If the pressure goes up to 20 mN/m, the multilayer condition happens as shown in Figure B-1(b). The wettability of the sample surface is also sensitive to the final coating quality. The superhydrophilic surface guarantees the good quality of the bead assembly. A successful monolayer coating of silica beads should look like a light blue color while observing at glazing angle regardless of the transparent or opaque substrate.

B.3 Hybrid Structure Fabrication

LYSO substrates were acquired from the Proteus Inc. with supply of different sizes and shape. The sample used here are all 2mm-thick due to the restriction of the vacuum chamber for deposition and etching. The entire fabrication is outlined here:

1. At EML, deposit a 500nm-thick Si_3N_4.

    - Plasmatherm PECVD for 70 min.
    - Flow rate: NH_3 3 sccm, SiH_4 100 sccm, N_2 600 sccm.
    - Pressure: 500 mtorr.
    - Power: 20W
    - Temperature: 250°C.
    - Deposition rate: ~7 nm/min.

    The index of refraction of the deposited Si_3N_4 as shown in Figure B-2 indicates no absorption of the deposited film.

2. At Prof. Nick Fang's lab, assemble monolayer using KSV NIMA 312. Please refer the previous sections for the beads preparation and coating process.

3. At NSL, spincoat ARC (XHRiC-16, Brewer Science Inc.).

    - 60 nm at 3500 rpm.

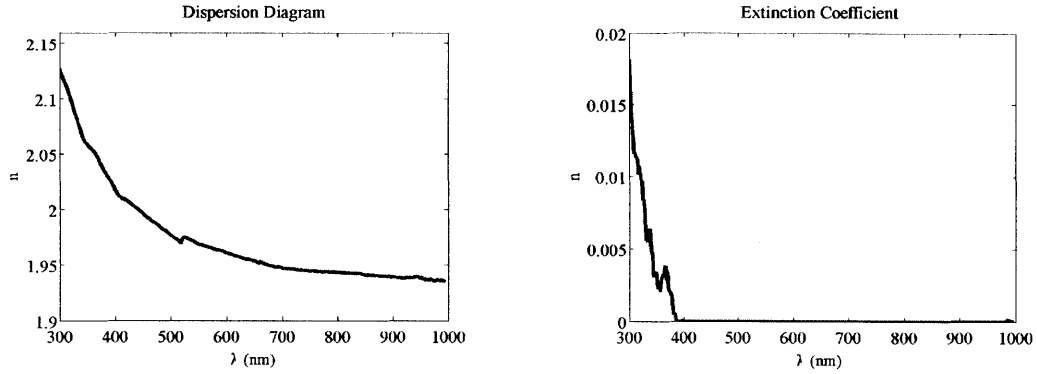

(a) (b)

Figure B-2: Optical property of the deposited Si_3N_4 (a) Dispersion (b) Extinction coefficient over the spectrum.

- Prebake at 180°C for 60 sec.

4. At NSL, spincoat 350 nm PR (PFI-88A2, Sumitomo Chemicals Corp.)
   - 350 nm at 900 rpm.
   - Prebake at 90°C for 90 sec.
5. At NSL, expose PR using laser interference lithography (Lloyd's mirror)
   - Power: 0.22 μW.
   - Exposure time: 2 min 15 sec for both horizontal and vertical axis.
   - Developer: CD-26 (2.4% Tetramethylammonium hydroxide, Rohm and Haas Electronic Materials LLC.) at rom temperature for 60 sec.
   - Post-bake PR at 110 °C for 90 sec.
6. At NSL, etch photonic slab
   - 15 min for 350 nm on Si_3N_4.
   - RIE Conditions: CF_4 20 sccm, 15 mtorr, and 150W .
7. At NSL, PR and ARC removal using asher at 150 W for 5 min.
8. At NSL, etch nanocone

- 5 min for 150 nm on Si_3N_4.
- RIE Conditions: CF_4 20 sccm, 15 mtorr, and 150 W.

B.4 Hybrid Structure Imprint

Imprinted hybrid structure uses the Si_3N_4 on Si substrate for molding the UV-cured polymer. The mold preparation is the same as previous section. Here, we begin the process from imprinted the hybrid structure. All processes can be done in NSL.

1. Activate the mold surface for high hydrophilicity using O_2 plasma for 3 min.
2. Silanize the mold by few PDMS drop (Poly(dimethylsiloxane), monoglycidyl ether terminated, Sigma-Aldrich Co.), and heat it up in 90°C oven for 4 hours.
3. Glass primer (CW 630713, Minuta Technology) drop on fused silica for better adhesion with resin. Wipe out the additional solution followed by 100°C baking on hotplate for 15 min.
4. Drops of 311RM polymer (MINS-311RM, Minuta Technology) on Si mold. Cover the treated surface of the fused silica toward the mold slowly in case of the generation of the bubbles.
5. Expose 311RM with light wavelength of 365 nm for 60s (lamp warm-up for 20 min before exposure).
6. Detach the mold from the fused silica.
7. Drops of ACW polymer (AC L2061-B, Addison Clear Wave Coating Inc.) on cured 311RM polymer followed by the LYSO stamping.
8. Expose ACW polymer with light wavelength of 365 nm for 3 min.

The imprinted hybrid structure is ready for characterization with grease coupling on fused silica side.

B.5 Point Spread Function Measurement for E-beam Writer

The process of the PSF measurement of e-beam writer is outlined here:

1. At TRL, deposit the SiO_2 and a-Si on bare Si wafer using STS-CVD.
2. At NSL, spin coat the HSQ.
    - 6% HSQ, XR1541-006 of Dow Corning.
    - 130 nm at 1000 rpm.
    - No pre-bake process for remaining the contrast.
3. At RLE, matrix dot exposure using SEBL.
    - 400 pA at Elionix ELS-F125.
    - Dose time starts from 0.1 μs with 1.2 times time increase.
    - Total 126 dots with 300 μm apart.
4. At NSL, develop the HSQ.
    - Salt developer (1 wt% NaOH and 4 wt% NaCl) for 4 min.
5. At RLE, imaging the exposure result using SEBL.
    - Raith 150 to imaging the diameter of exposed dots.
6. Using the function in [40] to fit the experimental dat using MATLAB.

Two example of the exposed dot are shown in Figure B-3. The exposed dot can fall down after development due to high aspect ratio at low dose condition. While dose increasing up to around nC, the exposed pattern becomes like a disk due to the dose from the scattering of secondary electrons.

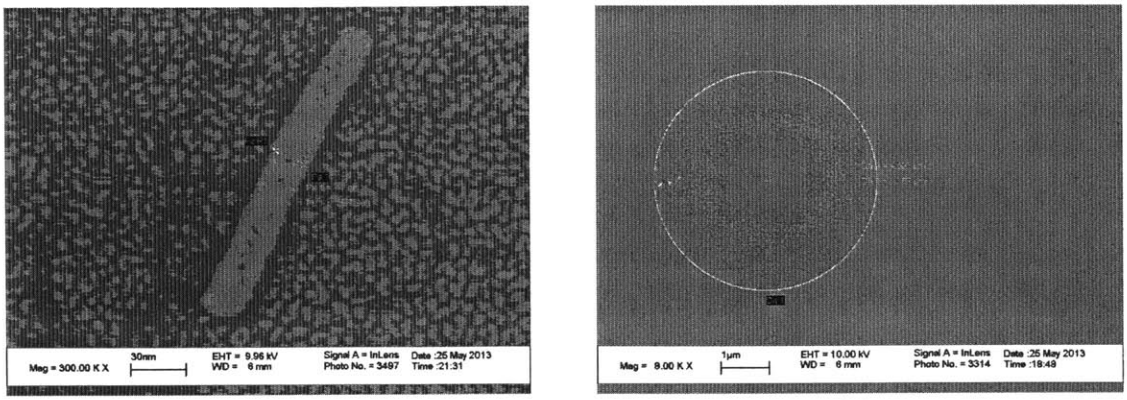

(a) (b)

Figure B-3: Point spread function measurement of e-beam writer by imaging the exposed rod diameter (a) Dose at 58.8 pC (the 40^{th} dot). Exposed dot fell down after development due to high aspect ratio (b) Dose at 11.8 μC (the 107^{th} dot). The HSQ becomes a disk pattern due to the scattering of secondary electrons.

B.6 Fabrication of Rod-slab Lünebug Lens

The process of the rod-slab Lünebug Lens is outlined here:

1. At TRL, deposit the SiO_2 and a-Si on bare Si wafer using STS-CVD.

2. At NSL, spin coat the HSQ.

   - 6% HSQ, XR1541-006 of Dow Corning.
   - 130nm at 1000 rpm.
   - No pre-bake process for remaining the contrast.

3. At RLE, write the pattern using SEBL.

   - 400 pA at Elionix ELS-F125.
   - Dose mean: 10600 $\mu C/cm^2$.

4. At NSL, develop the HSQ.

   - Salt developer (1 wt% NaOH and 4 wt% NaCl) for 4 min.

5. At EML, etch a-Si using Plasmatherm RIE.

- Flow rate: Cl_2 10 sccm, BCl_3 10 sccm, Ar 3 sccm.
- Pressure: 5 mtorr.
- Power: 80 W.
- Duration: 15 min.

B.7 Fabrication of Hole-slab Lünebug Lens

The process of the hole-slab Lünebug Lens is outlined here:

1. At TRL, deposit the SiO_2 and a-Si on bare Si wafer using STS-CVD.
   - HF-SIO2 and ASILICON recipe at STS-CVD.
   - Duration: 64 min and 23 min.
2. At NSL, spin coat the HSQ followed by ZEP-520A.
   - HSQ: FOX-14 of Dow Corning.
   - ZEP-520A: 1:1 copolymer of α-chloromethacrylate and α-methylstyrene, ZEON.
   - Both spun-on 130 nm at 6000 rpm.
   - Prebake both at 200°C for 3 min.
3. At RLE, write the pattern using SEBL.
   - 200 pA at Elionix ELS-F125.
   - Dose: 300 $\mu C/cm^2$.
4. At NSL, develop ZEP-520A.
   - *o*-xylene for 1 min.
   - Postbake at 100 °C for 3 min.
5. At NSL, etch the HSQ using RIE.

- Flow rate: CF_4 15 sccm.
- Pressure: 10 mtorr.
- Power: 150 W.
- Duration: 5 min.

6. At NSL, etch the a-Si using ICP-RIE.
   - Flow rate: $SiCl_4$ 10 sccm and Ar 6 sccm.
   - Pressure: 10 mtorr.
   - Power: ICP 200 W and bias 150 W.
   - Duration: 3 min.
7. At TRL, deposit the Si_3N_4 for passivation.
   - HF-SIN recipe at STS-CVD.
   - Duration: 2 min.

THIS PAGE INTENTIONALLY LEFT BLANK

Bibliography

[1] A. R. Knapitsch, "Photonic crystals: Enhancing the light output of scintillation based detectors," Ph.D. dissertation, CERN, 2012.

[2] Langmuir-blodgett method: http://eng.thesaurus.rusnano.com/wiki/article1797.

[3] Wilhelmy plate: http://en.wikipedia.org/wiki/wilhelmy-plate.

[4] S. Takahashi, C.-H. Chang, S. Y. Yang, and G. Barbastathis, "Design and fabrication of dielectric nanostructured luneburg lens in optical frequencies," in *International Conference on Optical MEMS and Nanophotonics (OMN).* IEEE Photonics Society, 2010, pp. 179–180.

[5] C.-H. Hsieh, *Wafer-level Moth-Eye Nanostructures Fabrication for Anti-reflection in Optoelectronic Devices.* Master thesis, National Tsing Hua University, 2007.

[6] C. M. Hsieh, J. Chyan, W.-C. Hsu, and J. A. Yeh, "Fabrication of wafer-level antireflective structures in optoelectronic applications," in *Optical MEMS and Nanophotonics, 2007 IEEE/LEOS International Conference on.* IEEE, 2007, pp. 185–186.

[7] H. Gao, F. Yan, Y. Zhang, J. Li, Y. Zeng, and G. Wang, "Enhancement of the light output power of ingan/gan light-emitting diodes grown on pyramidal patterned sapphire substrates in the micro-and nanoscale," *Journal of Applied Physics*, vol. 103, no. 1, p. 014314, 2008.

[8] Y. Lee, J. Hwang, T. Hsu, M. Hsieh, M. Jou, B. Lee, T. Lu, H. Kuo, and S. Wang, "Enhancing the output power of gan-based leds grown on wet-etched patterned sapphire substrates," *Photonics Technology Letters, IEEE*, vol. 18, no. 10, pp. 1152–1154, 2006.

[9] H. F. Ma and T. J. Cui, "Three-dimensional broadband and broad-angle transformation-optics lens," *Nat. Commun.*, vol. 1, p. 124, 2010.

[10] L. Gunderson and G. Holmes, "Microwave luneburg lens," *Appl. Opt.*, vol. 7, no. 5, pp. 801–804, 1968.

[11] C. Pfeiffer and A. Grbic, "A printed, broadband luneburg lens antenna," *IEEE Trans. Antennas. Propag.*, vol. 58, no. 9, pp. 3055–3059, 2010.

[12] S. Yao, D. Anderson, R. August, B. Youmans, and C. Oania, "Guided-wave optical thin-film luneburg lenses: fabrication technique and properties," *Applied optics*, vol. 18, no. 24, pp. 4067–4079, 1979.

[13] L. H. Gabrielli and M. Lipson, "Integrated luneburg lens via ultra-strong index gradient on silicon," *Opt. Express*, vol. 19, no. 21, pp. 20 122–20 127, Oct 2011.

[14] T. Zentgraf, Y. Liu, M. H. Mikkelsen, J. Valentine, and X. Zhang, "Plasmonic luneburg and eaton lenses," *Nat. Nanotechnol.*, vol. 6, no. 3, pp. 151–155, 2011.

[15] I. De Leon and P. Berini, "Amplification of long-range surface plasmons by a dipolar gain medium," *Nature Photonics*, vol. 4, no. 6, pp. 382–387, 2010.

[16] G. Woodside, *Environmental, safety, and health engineering.* John Wiley & Sons, 1997.

[17] M. S. Livingston and H. A. Bethe, "Nuclear physics c. nuclear dynamics, experimental," *Reviews of Modern Physics*, vol. 9, no. 3, p. 245, 1937.

[18] A. Knapitsch and P. Lecoq, "Review on photonic crystal coatings for scintillators," *International Journal of Modern Physics A*, 2014.

[19] M. Neviere, R. Petit, M. Cadilhac *et al.*, "Diffraction regimes of transmission gratings," *Bell Syst. Tech. J*, vol. 48, pp. 2909–2947, 1969.

[20] M. Moharam and T. K. Gaylord, "Diffraction analysis of dielectric surface-relief gratings," *JOSA*, vol. 72, no. 10, pp. 1385–1392, 1982.

[21] M. Moharam and L. Young, "Criterion for bragg and raman-nath diffraction regimes," *Applied optics*, vol. 17, no. 11, pp. 1757–1759, 1978.

[22] V. Liu and S. Fan, "S^4 : A free electromagnetic solver for layered periodic structures," *Computer Physics Communications*, vol. 183, no. 10, pp. 2233 – 2244, 2012.

[23] J. Allison, K. Amako, J. Apostolakis, H. Araujo, P. A. Dubois, M. Asai, G. Barrand, R. Capra, S. Chauvie, R. Chytracek *et al.*, "Geant4 developments and applications," *Nuclear Science, IEEE Transactions on*, vol. 53, no. 1, pp. 270–278, 2006.

[24] Slitrani, http://gentitfx.fr/slitrani/.

[25] C.-H. Chang, "Multilevel interference lithography–fabricating sub-wavelength periodic nanostructures," Ph.D. dissertation, Massachusetts Institute of Technology, 2008.

[26] W. Soppe, H. Rieffe, and A. Weeber, "Bulk and surface passivation of silicon solar cells accomplished by silicon nitride deposited on industrial scale by microwave pecvd," *Progress in photovoltaics: Research and applications*, vol. 13, no. 7, pp. 551–569, 2005.

[27] R. K. Luneberg, *Mathematical theory of optics.* Brown University Press, 1944.

[28] A. D. Falco, S. C. Kehr, and U. Leonhardt, "Luneburg lens in silicon photonics," *Opt. Express*, vol. 19, no. 6, pp. 5156–5162, Mar 2011.

[29] H. Gao, B. Zhang, S. G. Johnson, and G. Barbastathis, "Design of thin-film photonic metamaterial Lüneburg lens using analytical approach," *Opt. Express*, vol. 20, no. 2, pp. 1617–1628, Jan 2012.

[30] R. Bräuer and O. Bryngdahl, "Design of antireflection gratings with approximate and rigorous methods," *Applied optics*, vol. 33, no. 34, pp. 7875–7882, 1994.

[31] W. Yu, T. Konishi, T. Hamamoto, H. Toyota, T. Yotsuya, and Y. Ichioka, "Polarization-multiplexed diffractive optical elements fabricated by subwavelength structures," *Applied optics*, vol. 41, no. 1, pp. 96–100, 2002.

[32] J. D. Joannopoulos, S. G. Johnson, J. N. Winn, and R. D. Meade, *Photonic crystals: molding the flow of light.* Princeton university press, 2011.

[33] S. Johnson and J. Joannopoulos, "Block-iterative frequency-domain methods for maxwell's equations in a planewave basis," *Opt. Express*, vol. 8, no. 3, pp. 173–190, Jan 2001.

[34] A. F. Oskooi, D. Roundy, M. Ibanescu, P. Bermel, J. D. Joannopoulos, and S. G. Johnson, "Meep: A flexible free-software package for electromagnetic simulations by the fdtd method," *Comput. Phys. Commun.*, vol. 181, no. 3, pp. 687–702, 2010.

[35] C.-H. Hsieh, H. Gao, and G. Barbastathis, "Beam propagation of thin-film nanostructured lüneburg lens using hamiltonian ray- tracing and the wigner distribution function," in *Micro and Nano Engineering*, ser. Micro/Nano Devices for Physical Sciences and their Fabrication, September 2014.

[36] J. K. Yang and K. K. Berggren, "Using high-contrast salty development of hydrogen silsesquioxane for sub-10-nm half-pitch lithography," *Journal of Vacuum Science & Technology B*, vol. 25, no. 6, pp. 2025–2029, 2007.

[37] R. Sun, K. McComber, J. Cheng, D. K. Sparacin, M. Beals, J. Michel, and L. C. Kimerling, "Transparent amorphous silicon channel waveguides with silicon nitride intercladding layer," *Appl. Phys. Lett.*, vol. 94, no. 14, pp. 141 108–141 108, 2009.

[38] H. Jansen, H. Gardeniers, M. de Boer, M. Elwenspoek, and J. Fluitman, "A survey on the reactive ion etching of silicon in microtechnology," *J. Micromech. Microeng.*, vol. 6, no. 1, p. 14, 1996.

[39] S. Golka, M. Arens, M. Reetz, T. Kwapien, S. Bouchoule, and G. Patriarche, "Time-multiplexed, inductively coupled plasma process with separate sicl4 and o2 steps for etching of gaas with high selectivity," *Journal of Vacuum Science & Technology B*, vol. 27, no. 5, pp. 2270–2279, 2009.

[40] D. Winston, J. Ferrera, L. Battistella, A. Vladar, and K. Berggren, "Modeling the point-spread function in helium-ion lithography," *Scanning*, vol. 34, no. 2, pp. 121–128, 2012.

[41] T. Chang, "Proximity effect in electron-beam lithography," *Journal of Vacuum Science & Technology*, vol. 12, no. 6, pp. 1271–1275, 1975.

[42] M. J. Bastiaans, "The wigner distribution function applied to optical signals and systems," *Optics communications*, vol. 25, no. 1, pp. 26–30, 1978.

[43] ——, "New class of uncertainty relations for partially coherent light," *JOSA A*, vol. 1, no. 7, pp. 711–715, 1984.

[44] ——, "Application of the wigner distribution function to partially coherent light," *JOSA A*, vol. 3, no. 8, pp. 1227–1238, 1986.

[45] H. Gao, L. Tian, B. Zhang, and G. Barbastathis, "Iterative nonlinear beam propagation using hamiltonian ray tracing and wigner distribution function," *Opt. Lett.*, vol. 35, no. 24, pp. 4148–4150, Dec 2010.

[46] H. Gao, L. Tian, and G. Barbastathis, "Hamiltonian and phase-space representation of spatial solitons," *Optics Communications*, vol. 318, pp. 199–204, 2014.

[47] A. L. Rivera, S. M. Chumakov, and K. B. Wolf, "Hamiltonian foundation of geometrical anisotropic optics," *JOSA A*, vol. 12, no. 6, pp. 1380–1389, 1995.

[48] K. B. Wolf, *Geometric optics on phase space.* Springer, 2004.

[49] J. P. Mailoa, "Anti-reflection zinc oxide nanocones for higher efficiency thin-film silicon solar cells," Master's thesis, Massachusetts Institute of Technology, 2012.